Journal of Computational Physics 321 (2016) 414–434

Contents lists available at ScienceDirect

Journal of Computational Physics

www.elsevier.com/locate/jcp

An operator expansion method for computing nonlinear surface waves on a ferrofluid jet

Philippe Guyenne [a,b,*], Emilian I. Părău [c]

[a] Department of Mathematical Sciences, University of Delaware, Newark, DE 19716, USA
[b] Department of Mathematics and Computer Science, Faculty of Science, Chulalongkorn University, Bangkok 10330, Thailand
[c] School of Mathematics, University of East Anglia, Norwich, NR4 7TJ, UK

ARTICLE INFO

Article history:
Received 20 November 2015
Received in revised form 17 May 2016
Accepted 27 May 2016
Available online 31 May 2016

Keywords:
Dirichlet–Neumann operator
Ferrofluid jet
Pseudo-spectral method
Series expansion
Solitary waves

ABSTRACT

We present a new numerical method to simulate the time evolution of axisymmetric nonlinear waves on the surface of a ferrofluid jet. It is based on the reduction of this problem to a lower-dimensional computation involving surface variables alone. To do so, we describe the associated Dirichlet–Neumann operator in terms of a Taylor series expansion where each term can be efficiently computed by a pseudo-spectral scheme using the fast Fourier transform. We show detailed numerical tests on the convergence of this operator and, to illustrate the performance of our method, we simulate the long-time propagation and pairwise collisions of axisymmetric solitary waves. Both depression and elevation waves are examined by varying the magnetic field. Comparisons with weakly nonlinear predictions are also provided.

© 2016 Elsevier Inc. All rights reserved.

1. Introduction

Due to surface tension, it is well-known that an inviscid liquid jet (in the absence of gravity) is unstable to long-wave disturbances with wavelength greater than the jet circumference, eventually leading to the formation of disconnected droplets [35]. It has been observed however that a magnetic field can be used to suppress this Rayleigh instability for a jet composed of a ferrofluid [2].

Ferrofluids are colloidal liquids made of ferromagnetic nano-particles suspended in a carrier Newtonian fluid (e.g. an organic solvent or water). Therefore, in the presence of an external magnetic field, they become strongly magnetized and experience a body force. Ferrofluids have been a topic of intense research for the last few decades because of their potential commercial applications in various sectors. Industrial applications include 100% leak-free sealants, optical filters, heat sinks for loud speakers and transformers, viscous dampers, separators, magnetic fluid inks, actuators, acceleration and position probes, etc. [33]. There are also medical applications exploiting the extreme relative size difference between magnetic nano-particles and living cells. Examples include blood flow tracing in non-invasive circulatory measurements and magnetic drug targeting. In the latter case, the drugs would be enclosed by a ferrofluid layer and injected into the patient's body where they could be released at a specific location and time by turning off the magnetic field [36]. In addition, ferrofluids have been employed to study many intriguing phenomena and fundamental aspects of fluid mechanics, e.g. to obtain insight into colloidal forces and their role in the stabilization of colloidal suspensions, which has led to new applications for ferrofluid-based emulsions [31].

* Corresponding author at: Department of Mathematical Sciences, University of Delaware, Newark, DE 19716, USA. Tel.: +1 302 831 8664.
E-mail addresses: guyenne@udel.edu (P. Guyenne), e.parau@uea.ac.uk (E.I. Părău).

http://dx.doi.org/10.1016/j.jcp.2016.05.055
0021-9991/© 2016 Elsevier Inc. All rights reserved.

Of particular interest here is the set-up where a ferrofluid jet is exposed to an azimuthal magnetic field generated by a thin current-carrying wire positioned along the jet axis. The induced axisymmetric body force has a stabilizing effect and allows long-wave disturbances to develop on the jet surface [3,4]. In this configuration, Rannacher and Engel [34] confirmed via a linear stability analysis that the jet can indeed be stabilized and derived the cylindrical Korteweg–de Vries (KdV) equation describing axisymmetric weakly nonlinear disturbances in the long-wave limit. These authors identified soliton solutions to this model and showed that they are elevation waves (with a central hump) if $1 < B < 3/2$ and are depression waves (with a central dip) if $3/2 < B < 9$, where B denotes the magnetic Bond number. For $B < 1$, the jet is unstable [2]. More recently, Bourdin et al. [6] reported the first experimental observation of such axisymmetric waves and found a good agreement with the KdV predictions. Blyth and Părău [5] subsequently revisited this ferrofluid problem by solving the fully nonlinear equations numerically. After a hodograph transformation of these equations, a finite-difference scheme was used to discretize them over the entire fluid domain. Comparisons with results of [34] and [6] were made, and new nonlinear branches of solitary wave solutions were found. These include limiting cases such as a static wave with zero phase speed and overhanging waves with a trapped toroidal-shaped bubble. It should be pointed out however that [5] only computed steadily progressing solutions whose profile is fixed in a moving reference frame.

In the present paper, we extend the results of [34] and [5] by solving the full time-dependent nonlinear problem. For this purpose, we propose a new numerical approach based on the reduction of the original Laplace problem to a lower-dimensional system involving quantities evaluated only at the jet surface. No conformal or hodograph transformation is required, so the resulting equations are still written in terms of the physical Eulerian coordinates. This reduction is accomplished by introducing the Dirichlet–Neumann operator (DNO) which, in light of its analyticity properties, is expressed via a convergent Taylor series expansion about the uniform cylindrical geometry of the jet. Each term in this Taylor series is determined recursively as a sum of concatenations of Fourier multipliers with powers of the surface deformation, and thus is efficiently computed by a pseudo-spectral method using the fast Fourier transform. This computational efficiency is the key benefit of our surface formulation as compared to a volumetric one [5] and thus makes our numerical method particularly suitable for simulating the time evolution. Extensive numerical tests on the convergence of the DNO and on the accuracy of the time-integration scheme are provided. Although the present algorithm is applicable to a wide range of nonlinear wave phenomena, we focus here on solitary wave solutions, motivated by the above-mentioned literature. Numerical simulations of solitary wave collisions in various magnetic regimes are performed to illustrate their characteristics in this ferrofluid problem and to demonstrate the effectiveness of our numerical approach. Solutions from the finite-difference method of [5] are used to initialize our time-dependent computations, and the ensuing solitary wave collisions are compared with KdV predictions.

To our knowledge, this is the first time that such a numerical model is applied to investigating the present problem. In particular, the surface formulation as well as the derivation of the DNO in its series form and the corresponding numerical testing have previously never been reported for this axisymmetric cylindrical configuration. Earlier papers on DNO expansions have dealt with various examples from acoustics, electromagnetics and hydrodynamics featuring irregular domains [27,16,28,18,19] but they have only considered cases where the bulk equations and boundary conditions are linear in the field variables or where the reference geometry is rectangular with Cartesian coordinates. In addition, most of these previous studies only examined the time-harmonic regime and thus did not explicitly solve the time-evolution problem. The only exception that we are aware of is de la Llave and Panayotaros [17] who proposed a Hamiltonian formulation for nonlinear gravity waves on the surface of a sphere and derived a series expansion of the corresponding DNO in terms of spherical coordinates. This however was a theoretical work of different nature than ours and it did not produce any numerical result. As will be shown below, the series expansion of our DNO is established by using a harmonic solution to the Laplace equation whose form depends of course on the geometry of the problem. We also conduct here the first study of axisymmetric solitary wave collisions in the highly nonlinear regime and find notable qualitative differences compared to e.g. water waves in the classical rectangular configuration. This follows upon Bourdin et al.'s [6] conclusions suggesting that such a study would be of interest.

The remainder of the paper is organized as follows. In Section 2, we present the mathematical formulation of this axisymmetric ferrofluid problem, including the reduction to surface variables and the Taylor series expansion of the DNO. In Section 3, we describe the numerical methods for spatial and temporal discretization of the governing equations, including the procedures for generating the initial conditions, for de-aliasing and filtering. Section 4 shows numerical tests on the convergence of the DNO as well as applications to solitary waves, including their long-time propagation and pairwise collisions. Both depression and elevation waves are examined depending on B. Finally, concluding remarks are given in Section 5.

2. Mathematical formulation

2.1. Governing equations

Following Rannacher and Engel [34] and Blyth and Părău [5], we consider the inviscid, incompressible and irrotational flow of a liquid jet of density ρ along the outside of a cylindrical metal rod of radius b. The liquid flows in the z-direction of a cylindrical coordinate system (r, θ, z). Moreover, we assume conditions of axisymmetry so that all variables are independent of θ. In the basic steady configuration, the jet surface is a circular cylinder of radius $r = a$. The jet liquid is taken

to be a ferrofluid, i.e. a liquid that can be magnetized and thereby experience a body force in the presence of an external magnetic field. The axial rod carries a current I in the z-direction which generates an azimuthal magnetic field

$$\boldsymbol{B} = \frac{\mu_0 I \boldsymbol{e}_\theta}{2\pi r},$$

where $\boldsymbol{e}_\theta$ is the unit vector in the θ-direction. The magnetic field induces a radial body force per unit volume in the ferrofluid, given by

$$\boldsymbol{F} = \frac{\chi}{\mu_0}\boldsymbol{B}\cdot\nabla\boldsymbol{B} = -\frac{\mu_0\chi I^2}{4\pi^2 r^3}\boldsymbol{e}_r,$$

where $\boldsymbol{e}_r$ is the unit vector in the r-direction, χ is the magnetic susceptibility of the ferrofluid and $\mu_0 = 4\pi\times 10^{-7}\ \mathrm{H\,m^{-1}}$ is the magnetic permeability in a vacuum.

For convenience, we introduce the dimensionless spatial and temporal variables

$$\widetilde{r} = \frac{r}{a}, \qquad \widetilde{z} = \frac{z}{a}, \qquad \widetilde{t} = \sqrt{\frac{\gamma}{a^3\rho}}\,t,$$

where γ is the surface tension at the free surface of the jet. Dropping the tildes, the jet surface is located at $r = S(z,t) = 1+\eta(z,t)$, where η denotes the surface deformation relative to the basic configuration $r=1$. The flow in the ferrofluid is described by a velocity potential $\Phi(z,r,t)$ so that the velocity field is given by $\boldsymbol{u} = \nabla\Phi$. This velocity potential satisfies the Laplace equation

$$\nabla^2\Phi = 0, \qquad \text{for} \qquad z\in\mathbb{R}, \qquad b < r < S(z,t), \tag{1}$$

where $\nabla = (\partial_z, \partial_r)^\top$. At the axial rod $r=b$, a no-flux condition is imposed, namely

$$\partial_r\Phi = 0. \tag{2}$$

At the free surface $r = S(z,t)$, the two nonlinear boundary conditions are the kinematic condition

$$\partial_t S + (\partial_z\Phi)(\partial_z S) = \partial_r\Phi, \tag{3}$$

and the dynamic (or Bernoulli) condition

$$\partial_t\Phi + \frac{1}{2}|\nabla\Phi|^2 - \frac{\partial_z^2 S}{(1+(\partial_z S)^2)^{3/2}} + \frac{1}{S\sqrt{1+(\partial_z S)^2}} - 1 - \frac{B}{2}\left(\frac{1}{S^2}-1\right) = 0, \tag{4}$$

where

$$B = \frac{\mu_0\chi I^2}{4\pi^2\gamma a},$$

is the magnetic Bond number. To preserve the axial symmetry of the problem, gravity is neglected. The third, fourth and fifth terms on the left-hand side of (4) represent the capillary pressure, while the last group of terms involving B represents the magnetic stress. The two latter equations govern the time evolution of the jet surface.

Mass (or volume) as defined by

$$V = \int_{-\infty}^{\infty} \eta\, dz, \tag{5}$$

is a simple invariant of motion for (1)–(4), which will be established in a subsequent section. We remark however that Eq. (5) is not the actual volume integral in this axisymmetric cylindrical setting, which would be given by

$$W = \int_{-\infty}^{\infty}\int_0^{2\pi}\int_0^{1+\eta} r\,dr\,d\theta\,dz = \pi\int_{-\infty}^{\infty}(1+\eta)^2\,dz,$$

for $b=0$, or simply

$$W = \int_{-\infty}^{\infty}(1+\eta)^2\,dz, \tag{6}$$

if the coefficient π is omitted. Although not crucial, we may subtract unity from the integrand of (6) to ensure that the integral exists in the limit $\eta\to 0$. As shown below, our numerical simulations suggest that Eq. (6) is also an invariant of motion but we have no mathematical proof for this fact. Apart from these two quantities, we are unaware of any conserved energy for this system. Hereafter, for simplicity, we will restrict ourselves to the case $b=0$ corresponding to a very thin conducting rod, as in [3] and [34]. The more realistic case $0<b<1$ simply changes the geometry of the domain, would make the algebra more tedious and accordingly would lead to more complicated equations, but the proposed approach remains the same in principle.

2.2. Linearized problem

Because we are interested in waves propagating at the jet surface, we first examine the linearized problem. The dispersion relation for solutions of the form

$$S = 1 + \varepsilon A e^{\mathrm{i}(kz-\omega t)}, \qquad \Phi = \varepsilon f(r) e^{\mathrm{i}(kz-\omega t)},$$

where $\varepsilon \ll 1$ is a small parameter, and A and $f(r)$ are unknowns to be determined, reads

$$c^2 = \frac{(k^2+B-1)I_1(k)}{kI_0(k)}, \tag{7}$$

where I_0, I_1 are modified Bessel functions of the first kind and $c = \omega/k$ is the phase speed of linear waves. In the long-wave limit $k \to 0$, this phase speed reduces to

$$c_0 = \left(\frac{B-1}{2}\right)^{1/2}. \tag{8}$$

A key observation to be made from (7) is that the jet is unstable if $B < 1$, in which case there is a range of wavenumbers $k < \sqrt{1-B}$ for which c is purely imaginary and disturbances are amplified. If $B \geq 1$, then the wave speed c is real and neutral waves exist for arbitrary wavenumber k. It follows that a magnetic field of sufficient intensity can stabilize the Rayleigh capillary mode responsible for jet breakup under normal conditions [35]. Hence, the latter range of B is the regime of interest where we will look for nonlinear wave solutions. A more detailed linear analysis can be found in [34].

2.3. Surface formulation

Similarly to other free-surface flow problems such as water waves [16,14,20,38], we can reduce the dimensionality of the Laplace problem (1)–(4) by introducing

$$\xi(z,t) = \Phi(z, 1+\eta(z,t), t), \tag{9}$$

the trace of the velocity potential on the free surface $r = 1+\eta(z,t)$, together with the Dirichlet–Neumann operator (DNO)

$$G(\eta)\xi = \sqrt{1+(\partial_z\eta)^2}\,\partial_n\Phi\Big|_{r=1+\eta} = (-\partial_z\eta, 1)^\top \cdot \nabla\Phi\Big|_{r=1+\eta}, \tag{10}$$

which is the singular integral operator that takes Dirichlet data ξ on $r = 1+\eta(z,t)$, solves the Laplace equation (1) for Φ subject to (2), and returns the corresponding Neumann data (i.e. the normal velocity $\partial_n\Phi$ on the free surface). Note that $\partial_t S = \partial_t\eta$ and $\partial_z S = \partial_z\eta$. It is also pointed out that the DNO is linear in ξ but depends nonlinearly on η.

With these definitions, we are able to express the boundary conditions (3)–(4) in terms of surface variables alone. Recall that the jet surface is where the dynamics of interest takes place. In particular, all the spatial and temporal derivatives of Φ on $r = 1+\eta(z,t)$ can be explicitly written in terms of η and ξ (and their derivatives) together with $G(\eta)\xi$. For this purpose, we use a number of identities namely

$$\partial_t\xi = \partial_t\Phi + (\partial_r\Phi)(\partial_t\eta)\Big|_{r=1+\eta}, \qquad \partial_z\xi = \partial_z\Phi + (\partial_r\Phi)(\partial_z\eta)\Big|_{r=1+\eta}, \tag{11}$$

by differentiating (9) and using the chain rule, as well as

$$G(\eta)\xi = \partial_r\Phi - (\partial_z\Phi)(\partial_z\eta)\Big|_{r=1+\eta},$$

by virtue of (10). This implies

$$\partial_z\Phi = \partial_z\xi - (\partial_r\Phi)(\partial_z\eta)\Big|_{r=1+\eta}, \tag{12}$$

and

$$\begin{aligned}\partial_r\Phi &= G(\eta)\xi + (\partial_z\Phi)(\partial_z\eta) = G(\eta)\xi + \Big[\partial_z\xi - (\partial_r\Phi)(\partial_z\eta)\Big](\partial_z\eta)\Big|_{r=1+\eta},\\ &= G(\eta)\xi + (\partial_z\xi)(\partial_z\eta) - (\partial_r\Phi)(\partial_z\eta)^2\Big|_{r=1+\eta},\end{aligned}$$

which yields

$$\partial_r\Phi\Big|_{r=1+\eta} = \frac{1}{1+(\partial_z\eta)^2}\Big[G(\eta)\xi + (\partial_z\xi)(\partial_z\eta)\Big]. \tag{13}$$

Then, by substituting (13) back into (12) and (11), we obtain

$$\partial_z\Phi\Big|_{r=1+\eta} = \partial_z\xi - \frac{\partial_z\eta}{1+(\partial_z\eta)^2}\Big[G(\eta)\xi + (\partial_z\xi)(\partial_z\eta)\Big],$$
$$= \frac{1}{1+(\partial_z\eta)^2}\Big[\partial_z\xi - (\partial_z\eta)G(\eta)\xi\Big], \tag{14}$$

and

$$\partial_t\Phi = \partial_t\xi - (\partial_r\Phi)(\partial_t\eta)\Big|_{r=1+\eta},$$
$$= \partial_t\xi - \frac{G(\eta)\xi}{1+(\partial_z\eta)^2}\Big[G(\eta)\xi + (\partial_z\xi)(\partial_z\eta)\Big].$$

For the latter equation, we have also used the fact that

$$\partial_t\eta = \partial_r\Phi - (\partial_z\Phi)(\partial_z\eta)\Big|_{r=1+\eta} = G(\eta)\xi\,,$$

according to the kinematic condition (3) and the definition (10) of the DNO. Moreover, adding up the squares of (13) and (14),

$$(\partial_r\Phi)^2\Big|_{r=1+\eta} = \frac{1}{(1+(\partial_z\eta)^2)^2}\Big[(G(\eta)\xi)^2 + 2(\partial_z\eta)(\partial_z\xi)G(\eta)\xi + (\partial_z\eta)^2(\partial_z\xi)^2\Big],$$

$$(\partial_z\Phi)^2\Big|_{r=1+\eta} = \frac{1}{(1+(\partial_z\eta)^2)^2}\Big[(\partial_z\xi)^2 - 2(\partial_z\eta)(\partial_z\xi)G(\eta)\xi + (\partial_z\eta)^2(G(\eta)\xi)^2\Big],$$

leads to

$$(\partial_z\Phi)^2 + (\partial_r\Phi)^2\Big|_{r=1+\eta} = \frac{1}{(1+(\partial_z\eta)^2)^2}\Big[(1+(\partial_z\eta)^2)(\partial_z\xi)^2 + (1+(\partial_z\eta)^2)(G(\eta)\xi)^2\Big],$$
$$= \frac{1}{1+(\partial_z\eta)^2}\Big[(\partial_z\xi)^2 + (G(\eta)\xi)^2\Big].$$

Inserting these expressions in (3)–(4) gives a closed system of two equations

$$\partial_t\eta = G(\eta)\xi\,, \tag{15}$$
$$\partial_t\xi = -\frac{1}{2(1+(\partial_z\eta)^2)}\Big[(\partial_z\xi)^2 - 2(\partial_z\eta)(\partial_z\xi)G(\eta)\xi - (G(\eta)\xi)^2\Big] \tag{16}$$
$$+ \frac{\partial_z^2\eta}{(1+(\partial_z\eta)^2)^{3/2}} - \frac{1}{(1+\eta)\sqrt{1+(\partial_z\eta)^2}} + 1 + \frac{B}{2}\left[\frac{1}{(1+\eta)^2} - 1\right],$$

for the two surface variables η and ξ, which is completely equivalent to the original formulation (1)–(4). Recall that, by construction, the solution of the Laplace equation (1) subject to the no-flux condition (2) at $r=0$ is encoded in the DNO. Details are provided in the next section.

2.4. Dirichlet–Neumann operator

As shown by Coifman and Meyer [8], Craig et al. [15] and Craig [9] for data defined on the whole hyperplane, and by Nicholls and Reitich [29] and Hu and Nicholls [25] for periodic data, the DNO has a number of properties including:

(i) it is self-adjoint,
(ii) it is analytic in η,

under certain (relatively mild) regularity conditions on the free surface (say $\eta \in C^1$). It is reasonable to assume that these properties hold in our axisymmetric cylindrical configuration although we leave the details of their rigorous analysis outside the scope of this paper. We refer the interested reader to [28] and [18] who rigorously established the analyticity of the DNO in the two-dimensional circular and three-dimensional spherical settings, respectively.

Property (i) can be used to easily prove the conservation of V in time as stated above. We first remark that $G(\eta)1 = 0$ which directly follows from the definition (10) of the DNO by substituting Φ with 1. From (5), we have

$$\frac{dV}{dt} = \int_{-\infty}^{\infty} \partial_t\eta\, dz\,.$$

Then using (15) and integrating by parts lead to

$$\frac{dV}{dt} = \int_{-\infty}^{\infty} G(\eta)\xi \, dz = \int_{-\infty}^{\infty} \xi \, G(\eta)1 \, dz = 0 \, .$$

The question now is, given η and ξ at time t, how to evaluate $G(\eta)\xi$ so that Eqs. (15)–(16) can be completed and then solved. To this aim, we proceed as outlined earlier when defining the DNO. Considering harmonic functions of the form $\Phi = f(r)e^{\mathrm{i}kz}$ associated with wave propagation in the z-direction, where the t-dependence is omitted since the domain is fixed at a given time, and inserting this expression into (1) yield the modified Bessel's equation

$$\kappa^2 f'' + \kappa f' - \kappa^2 f = 0 \, , \tag{17}$$

where $\kappa = kr$ and the primes represent differentiation with respect to κ. The general solution of (17) can be written as a linear combination of modified Bessel functions of the first and second kinds, I_0 and K_0 respectively. Here we only need to consider I_0 because the no-flux condition (2) at $r = 0$ cannot be enforced with K_0. Hence the choice of harmonic solution

$$\Phi = I_0(kr)e^{\mathrm{i}kz} \, , \tag{18}$$

is sufficient for the purposes of our derivation since the DNO is linear in ξ. It readily follows from (18) that

$$\partial_r \Phi = kI_0'(kr)e^{\mathrm{i}kz} = kI_1(kr)e^{\mathrm{i}kz} \, , \qquad \partial_z \Phi = \mathrm{i}kI_0(kr)e^{\mathrm{i}kz} \, ,$$

which confirms that $\partial_r \Phi|_{r=0} \sim I_1(0) = 0$. An extensive review on the modified Bessel functions and their properties can be found in e.g. [1].

Next we will take advantage of the analyticity property (ii) to derive a Taylor series expansion in η,

$$G(\eta) = \sum_{j=0}^{\infty} G_j(\eta) \, , \tag{19}$$

for evaluating the DNO. Each term G_j in (19) is homogeneous of degree j in η, and thus its action on the basis function $e^{\mathrm{i}kz}$ can be characterized recursively in the following way. Substituting (18) and (19) into (10) gives

$$\Big(\sum_{j=0}^{\infty} G_j(\eta)\Big) I_0\big(k(1+\eta)\big)e^{\mathrm{i}kz} = \Big[I_1\big(k(1+\eta)\big) - \mathrm{i}(\partial_z \eta) I_0\big(k(1+\eta)\big)\Big] k e^{\mathrm{i}kz} \, ,$$

which becomes

$$\Big(\sum_{j=0}^{\infty} G_j(\eta)\Big)\Big(\sum_{n=0}^{\infty} \frac{(k\eta)^n}{n!} I_0^{(n)}(k)\Big)e^{\mathrm{i}kz} = \sum_{n=0}^{\infty} \frac{(k\eta)^n}{n!}\Big[I_1^{(n)}(k) - \mathrm{i}(\partial_z \eta) I_0^{(n)}(k)\Big] k e^{\mathrm{i}kz} \, ,$$

after Taylor expanding $I_0\big(k(1+\eta)\big)$ and $I_1\big(k(1+\eta)\big)$ about $\eta = 0$. The functions $I_0^{(n)}$, $I_1^{(n)}$ denote the n-th derivatives of I_0, I_1 with respect to their arguments. Then identifying terms of the same degree in η provides a recursion formula for the various G_j's in (19). For $j = 0$ (i.e. $\eta = 0$), we obtain

$$G_0(0) I_0(k) e^{\mathrm{i}kz} = kI_1(k)e^{\mathrm{i}kz} \, , \qquad \text{so} \qquad G_0(0)e^{\mathrm{i}kz} = \frac{kI_1(k)}{I_0(k)} e^{\mathrm{i}kz} \, ,$$

which can be viewed as the Fourier symbol of the pseudo-differential operator

$$G_0(0) = \frac{DI_1(D)}{I_0(D)} \, ,$$

acting in the physical z-space, where $D = -\mathrm{i}\partial_z$ is defined in such a way that its Fourier symbol is k (the factor i represents the imaginary unit). Note that $I_0(0) = 1 \neq 0$ for $k = 0$, so G_0 is well-defined for all values of k. The pseudo-differential operators D and G_0 are also called Fourier multipliers due to their multiplicative action in the Fourier k-space.

Similarly, for $j > 0$, we find

$$\begin{aligned} G_j(\eta) &= \frac{1}{j!}(k\eta)^j k \frac{I_1^{(j)}(k)}{I_0(k)} - \frac{1}{(j-1)!}(\mathrm{i}\partial_z \eta)(k\eta)^{j-1} k \frac{I_0^{(j-1)}(k)}{I_0(k)} - \sum_{\ell=0}^{j-1} \frac{1}{(j-\ell)!} G_\ell(\eta)(k\eta)^{j-\ell} \frac{I_0^{(j-\ell)}(k)}{I_0(k)} \, , \\ &= \left(\frac{1}{j!}\eta^j k^{j+1} + \frac{1}{(j-1)!}(D\eta)\eta^{j-1}k^j\right)\frac{I_0^{(j-1)}(k)}{I_0(k)} + \frac{1}{j!}\eta^j k^{j+1}\left(\frac{I_1^{(j)}(k) - I_0^{(j-1)}(k)}{I_0(k)}\right) \\ &\quad - \sum_{\ell=0}^{j-1} \frac{1}{(j-\ell)!} G_\ell(\eta)\eta^{j-\ell}k^{j-\ell}\frac{I_0^{(j-\ell)}(k)}{I_0(k)} \, , \end{aligned}$$

and again its action in the physical space can be formulated in terms of D as

$$G_j(\eta) = \frac{1}{j!} D\eta^j D^j \frac{I_0^{(j-1)}(D)}{I_0(D)} + \frac{1}{j!}\eta^j D^{j+1}\left(\frac{I_1^{(j)}(D) - I_0^{(j-1)}(D)}{I_0(D)}\right) - \sum_{\ell=0}^{j-1} \frac{1}{(j-\ell)!} G_\ell(\eta)\eta^{j-\ell} D^{j-\ell} \frac{I_0^{(j-\ell)}(D)}{I_0(D)}, \tag{20}$$

after noting that

$$\frac{1}{j!} D\eta^j D^j = \frac{1}{j!}\eta^j D^{j+1} + \frac{1}{(j-1)!}(D\eta)\eta^{j-1} D^j.$$

For example, the first two contributions from (20) are

$$\begin{aligned} G_1(\eta) &= D\eta D + \eta D^2\left(\frac{I_1'(D) - I_0(D)}{I_0(D)}\right) - G_0\eta D\frac{I_0'(D)}{I_0(D)}, \\ &= D\eta D - G_0\eta G_0 - \eta G_0, \end{aligned} \tag{21}$$

since

$$I_0'(D) = I_1(D), \qquad I_1'(D) = I_0(D) - D^{-1} I_1(D),$$

and

$$\begin{aligned} G_2(\eta) &= \frac{1}{2} D\eta^2 D^2 \frac{I_0'(D)}{I_0(D)} + \frac{1}{2}\eta^2 D^3\left(\frac{I_1''(D) - I_0'(D)}{I_0(D)}\right) - \frac{1}{2} G_0\eta^2 D^2 \frac{I_0''(D)}{I_0(D)} - G_1\eta D\frac{I_0'(D)}{I_0(D)}, \\ &= \frac{1}{2} D\eta^2 D G_0 + \frac{1}{2}\eta^2 D^2 G_0 - \frac{1}{2}\eta^2 D^2 + \eta^2 G_0 - \frac{1}{4} G_0\eta^2 D^2 - \frac{1}{4} G_0\eta^2 D^2 \frac{I_2(D)}{I_0(D)} - G_1\eta G_0, \end{aligned} \tag{22}$$

since

$$I_0''(D) = \frac{1}{2}\Big(I_0(D) + I_2(D)\Big), \qquad I_1''(D) = \Big(1 + 2D^{-2}\Big) I_1(D) - D^{-1} I_0(D).$$

By virtue of the self-adjointness property (i), the order of application of the various operators in (20) can be switched to arrive at

$$G_j(\eta) = \frac{1}{j!}\frac{I_0^{(j-1)}(D)}{I_0(D)} D^j\eta^j D + \frac{1}{j!}\eta^j D^{j+1}\left(\frac{I_1^{(j)}(D) - I_0^{(j-1)}(D)}{I_0(D)}\right) - \sum_{\ell=0}^{j-1} \frac{1}{(j-\ell)!}\frac{I_0^{(j-\ell)}(D)}{I_0(D)} D^{j-\ell}\eta^{j-\ell} G_\ell(\eta). \tag{23}$$

Equation (23) forms the basis of our numerical method to compute the DNO and thus to solve (15)–(16). As pointed out by Craig and Nicholls [14] and Xu and Guyenne [38], the adjoint recursion formula (23) is equivalent to (20) but it is computationally more efficient since it allows us to save and re-use the G_j's as vector operations on ξ, without having to re-compute them at each order j when applied to concatenations of Fourier multipliers and powers of η. The various derivatives of I_0 and I_1 in (23) can be calculated as linear combinations of modified Bessel functions, namely

$$\begin{aligned} I_0^{(n)}(D) &= \frac{1}{2^n}\sum_{m=0}^{n} C_m^n I_{2m-n}(D), \\ &= \frac{1}{2^n}\Big[C_0^n I_{-n}(D) + C_1^n I_{2-n}(D) + \cdots + C_n^n I_n(D)\Big], \end{aligned} \tag{24}$$

and

$$\begin{aligned} I_1^{(n)}(D) &= \frac{1}{2^n}\sum_{m=0}^{n} C_m^n I_{2m+1-n}(D), \\ &= \frac{1}{2^n}\Big[C_0^n I_{1-n}(D) + C_1^n I_{3-n}(D) + \cdots + C_n^n I_{1+n}(D)\Big], \end{aligned} \tag{25}$$

where

$$C_m^n = \frac{n!}{m!(n-m)!},$$

represents the binomial coefficient [1, Chap. 9]. The values of modified Bessel functions of the first kind are tabulated; for example, these functions are denoted by the command *besseli* in Matlab.

It should be pointed out that the surface formulation (15)–(16) together with the series expansion (19) of the DNO require that the free surface η be a single-valued graph of z. Therefore, overturning waves (with a multi-valued profile) are not permitted with the present algorithm.

3. Numerical methods

3.1. Space discretization

For space discretization, we assume periodic boundary conditions in z (with $z_{\min} \le z \le z_{\max}$) and use a pseudo-spectral method based on the fast Fourier transform (FFT). This is a particularly suitable choice for the computation of the DNO since each term (23) in its Taylor series expansion consists of concatenations of Fourier multipliers with powers of η.

More specifically, both functions η and ξ are expanded in truncated Fourier series

$$\begin{pmatrix} \eta \\ \xi \end{pmatrix} = \sum_k \begin{pmatrix} \widehat{\eta}_k \\ \widehat{\xi}_k \end{pmatrix} e^{\mathrm{i}kz}.$$

Spatial derivatives and Fourier multipliers are evaluated in the Fourier space, while nonlinear products are calculated in the physical space on a regular grid of N collocation points [7]. For example, if we wish to apply the zeroth-order operator G_0 to a function ξ in the physical space, we first transform ξ to the Fourier space via FFT, apply the diagonal operator $kI_1(k)/I_0(k)$ to the Fourier coefficients $\widehat{\xi}_k$ of ξ, and then transform back to the physical space.

In practice, the Taylor series of the DNO is also truncated to a finite number of terms,

$$G(\eta) \approx G^M(\eta) = \sum_{j=0}^{M} G_j(\eta), \tag{26}$$

where the truncation order M is chosen according to the physical regime under consideration and/or the level of accuracy desired. In its adjoint form (23), the computational cost for evaluating (26) is estimated to be $O(M^2 N \log N)$ by using the FFT. The choice of M will be discussed in more detail below but, thanks to the analyticity property (ii), it is usually sufficient to select a relatively small number of terms ($M < 10 \ll N$) for satisfactory results. This cost estimate is an indicator of how efficient our numerical method potentially is as compared to other elliptic solvers such as boundary-integral methods or volumetric finite-difference/element methods.

3.2. De-aliasing and ill-conditioning

Two major sources of numerical error in the present algorithm are aliasing and ill-conditioning. Typically the larger the wave amplitude or steepness, the more significant these effects. Aliasing is inherent to the pseudo-spectral approach when applied to nonlinear equations [32]. As commonly observed in operator expansion methods [30], ill-conditioning is related to the evaluation of the DNO in its series form (26) which relies heavily on cancellations of terms to ensure convergence. In practice, terms are not canceled exactly due to round-off errors which are then amplified through the recursive process, most severely in the highest Fourier modes, to eventually ruin the accuracy of the numerical calculation. As shown in (23), the presence of many Fourier multipliers D^j (equivalent to derivatives) whose order increases with the series order, can dramatically amplify numerical errors and thus may promote numerical instabilities during the time evolution. This ill-conditioning issue will be discussed in more detail below when presenting numerical tests.

Here aliasing occurs primarily in the computation of the DNO. The j-term $G_j\xi$ in (26) involves nonlinearities of order $j+1$, so aliasing errors may accumulate quickly for large j. Complete de-aliasing may be achieved by the zero-padding technique which, for the DNO truncated at order M, requires increasing the size of the spectra of η and ξ by a factor of up to $M+1$. The extra modes are then set to zero to prevent aliasing errors from arising. In fact, since the FFT is used, the nearest power of 2 greater than or equal to $M+1$ should be chosen. This de-aliasing procedure was also used in [10,38] and [21,22] for simulations of gravity and flexural-gravity waves. Note that it is accompanied by an increase in computer memory storage and run time but, in the present axisymmetric situation, this was not found to be a serious issue.

3.3. Time integration

Time integration of (15)–(16) is performed in the Fourier space so that the linear terms can be solved exactly by the integrating factor technique, thus lessening the stiffness of the problem [7,16,12]. For this purpose, we first separate the linear and nonlinear parts in (15)–(16). Defining $\boldsymbol{v} = (\eta, \xi)^\top$, these equations can be expressed as

$$\partial_t \boldsymbol{v} = \mathcal{L}\boldsymbol{v} + \mathcal{N}(\boldsymbol{v}), \tag{27}$$

where the linear part $\mathcal{L}$ is defined by

$$\mathcal{L}\boldsymbol{v} = \begin{pmatrix} 0 & G_0 \\ \partial_z^2 + 1 - B & 0 \end{pmatrix} \begin{pmatrix} \eta \\ \xi \end{pmatrix},$$

with $\partial_z^2\eta + (1-B)\eta$ being the leading-order linear contributions from the capillary and magnetic terms in (16), and the nonlinear part $\mathcal{N} = (\mathcal{N}_1, \mathcal{N}_2)^\top$ is given by

$$\mathcal{N}_1 = \big(G(\eta) - G_0\big)\xi\,,$$

$$\mathcal{N}_2 = -\frac{1}{2(1+(\partial_z\eta)^2)}\Big[(\partial_z\xi)^2 - 2(\partial_z\eta)(\partial_z\xi)G(\eta)\xi - (G(\eta)\xi)^2\Big] - \partial_z^2\eta + \frac{\partial_z^2\eta}{(1+(\partial_z\eta)^2)^{3/2}} - \eta - \frac{1}{(1+\eta)\sqrt{1+(\partial_z\eta)^2}} + 1 + B\eta + \frac{B}{2}\left[\frac{1}{(1+\eta)^2} - 1\right].$$

Subtraction of the terms $G_0\xi$ in $\mathcal{N}_1$ and $\partial_z^2\eta + (1-B)\eta$ in $\mathcal{N}_2$ is meant to compensate for their presence in the linear part $\mathcal{L}\boldsymbol{v}$. Then, by taking the Fourier transform of (27) and making the change of variables

$$\widehat{\boldsymbol{v}}_k(t) = \Theta(t)\widehat{\boldsymbol{w}}_k(t)\,, \tag{28}$$

where

$$\Theta(t) = \begin{pmatrix} \cos\big(t\sqrt{(k^2+B-1)G_0}\big) & \sqrt{\frac{G_0}{k^2+B-1}}\sin\big(t\sqrt{(k^2+B-1)G_0}\big) \\ -\sqrt{\frac{k^2+B-1}{G_0}}\sin\big(t\sqrt{(k^2+B-1)G_0}\big) & \cos\big(t\sqrt{(k^2+B-1)G_0}\big) \end{pmatrix},$$

we obtain the following nonlinear system

$$\partial_t\widehat{\boldsymbol{w}}_k = \Theta(t)^{-1}\widehat{\mathcal{N}}_k\big[\Theta(t)\widehat{\boldsymbol{w}}_k\big],$$

for $\widehat{\boldsymbol{w}}_k$, which is solved numerically in time using the fourth-order Runge–Kutta scheme with constant step Δt. In terms of the original variables $\widehat{\boldsymbol{v}}_k$, by inverting (28), this scheme reads

$$\widehat{\boldsymbol{v}}_k^{n+1} = \Theta(\Delta t)\widehat{\boldsymbol{v}}_k^n + \frac{\Delta t}{6}\Theta(\Delta t)\big(f_1 + 2f_2 + 2f_3 + f_4\big), \tag{29}$$

where

$$f_1 = \widehat{\mathcal{N}}_k\big(\widehat{\boldsymbol{v}}_k^n\big),$$
$$f_2 = \Theta\left(-\frac{\Delta t}{2}\right)\widehat{\mathcal{N}}_k\left[\Theta\left(\frac{\Delta t}{2}\right)\left(\widehat{\boldsymbol{v}}_k^n + \frac{\Delta t}{2}f_1\right)\right],$$
$$f_3 = \Theta\left(-\frac{\Delta t}{2}\right)\widehat{\mathcal{N}}_k\left[\Theta\left(\frac{\Delta t}{2}\right)\left(\widehat{\boldsymbol{v}}_k^n + \frac{\Delta t}{2}f_2\right)\right],$$
$$f_4 = \Theta(-\Delta t)\widehat{\mathcal{N}}_k\big[\Theta(\Delta t)\big(\widehat{\boldsymbol{v}}_k^n + \Delta t f_3\big)\big],$$

for the solution at time $t_{n+1} = t_n + \Delta t$. The integrating factor $\Theta(t)$ is the fundamental matrix of the linear system

$$\partial_t\widehat{\boldsymbol{v}}_k = \widehat{\mathcal{L}}_k\widehat{\boldsymbol{v}}_k = \begin{pmatrix} 0 & G_0 \\ 1-B-k^2 & 0 \end{pmatrix}\begin{pmatrix} \widehat{\eta}_k \\ \widehat{\xi}_k \end{pmatrix},$$

and, in the limit $k \to 0$, it reduces to

$$\Theta(t) = \begin{pmatrix} 1 & 0 \\ -(B-1)t & 1 \end{pmatrix},$$

as given by l'Hôpital's rule. In establishing (29), we have used the fact that $\Theta(t)$ is a semigroup and satisfies

$$\Theta(a+b) = \Theta(a)\Theta(b)\,, \qquad \Theta^{-1}(a) = \Theta(-a)\,.$$

These identities can be easily checked by direct calculation. Note that the coefficient of t in the argument of the cosine and sine functions for the fundamental matrix $\Theta(t)$ is nothing but the linear dispersion relation in terms of the angular frequency

$$\omega = \sqrt{(k^2+B-1)G_0} = \sqrt{\frac{(k^2+B-1)kI_1(k)}{I_0(k)}},$$

which is related to the phase speed (7) by $\omega = ck$.

3.4. Filtering and initial condition

In our simulations, we have typically used $\Delta t = 0.001$ as a good compromise between accuracy, stability and computational cost. For reference, this time step is thousands times smaller than the linear wave period $\tau = 2\pi/\omega \simeq 6$ for $B = 2.5$ and $k = 1$. Given the fourth-order accuracy of our time-integration scheme, this value of Δt is quite reasonable. We have also observed that using a smaller time step does not generally yield much better results partly because, to reach the same simulation time, more computations of the DNO are required, thus introducing more numerical errors.

In the case of large-amplitude or highly deformed waves, we have found it necessary to apply filtering in order to stabilize the numerical solution so that it can be computed over a sufficiently long time. Otherwise, spurious high-wavenumber instabilities tend to develop, eventually leading to the computation breakdown. This issue may be related to ill-conditioning of the DNO as mentioned earlier (which will be further discussed in Section 4.1) but it may also be related to the specific nonlinearity and stiffness of the problem, hence use of prohibitively small time steps may be required to ensure stability. As a remedy, we apply a hyperviscosity-type filter of the form

$$\exp\left(-36\left|\frac{k}{k_{\max}}\right|^{36}\right),$$

to the Fourier coefficients $\widehat{\eta}_k$ and $\widehat{\xi}_k$ at each time step, where $k_{\max}$ is the largest wavenumber of the resolved spectrum. Such a filter has been commonly employed in direct numerical simulations of nonlinear fluid flows by spectral methods [7,24,23,38] and its form ensures that only energy levels at high wavenumbers are significantly affected. Therefore, if a sufficiently fine resolution is specified, this filtering procedure should be able to suppress instabilities while preserving the overall solution.

To initialize our simulations of (15)–(16) for solitary waves, we use the finite-difference method of Blyth and Părău [5] which computes such solutions in a reference frame moving with the wave speed. For the reader's convenience, we present a brief description of their finite-difference method in the next section and refer to their paper for more details.

3.5. Finite-difference method for solitary waves

Solitary waves traveling at constant speed $c > 0$ are considered. In a reference frame moving with speed c, the boundary conditions (3) and (4) at the free surface $r = S(Z) = 1 + \eta(Z)$ where $Z = z - ct$, become

$$\partial_r \Phi = (\partial_Z \Phi)(\partial_Z \eta),$$

and

$$\frac{1}{2}(\partial_Z \Phi)^2\Big[1 + (\partial_Z \eta)^2\Big] - \frac{\partial_Z^2 \eta}{(1 + (\partial_Z \eta)^2)^{3/2}} + \frac{1}{(1+\eta)\sqrt{1 + (\partial_Z \eta)^2}} - \frac{B}{2(1+\eta)^2}$$
$$= \frac{1}{2}c^2 + 1 - \frac{B}{2}.$$

To compute solitary waves on an axisymmetric jet, we employ the numerical method initially described by Jeppson [26] and subsequently used by Vanden-Broeck et al. [37] for capillary waves. It is based on finite differences and requires solving for the unknowns $r(\Phi, \psi)$ and $z(\Phi, \psi)$ in the inverse plane (Φ, ψ), where ψ is the Stokes streamfunction defined as

$$-\frac{\partial_Z \psi}{r} = \partial_r \Phi, \qquad \frac{\partial_r \psi}{r} = \partial_Z \Phi.$$

The advantage of this approach is that the fluid domain is rectangular and fixed in the inverse plane, as given by

$$-\infty < \Phi < \infty, \qquad 0 \le \psi \le \psi_S,$$

where $\psi_S = c/2$. The derivatives of the new unknowns can be written as

$$\partial_\psi Z = -\frac{\partial_\Phi r}{r}, \qquad \partial_\psi r = \frac{\partial_\Phi Z}{r}. \tag{30}$$

In terms of these new variables, the Laplace equation (1) becomes

$$r^3(\partial_\psi^2 r) + r(\partial_\Phi^2 r) + r^2(\partial_\psi r)^2 - (\partial_\Phi r)^2 = 0, \tag{31}$$

and the Bernoulli condition at $\psi = \psi_S$ reads

$$\frac{1/2}{r^2(\partial_\psi r)^2 + (\partial_\Phi r)^2} - \frac{r(\partial_\psi r)(\partial_\Phi^2 r) - (\partial_\Phi r)^2(\partial_\psi r) - r(\partial_\Phi r)(\partial_{\Phi\psi}^2 r)}{\big[(\partial_\Phi r)^2 + r^2(\partial_\psi r)^2\big]^{3/2}}$$
$$-\frac{|\partial_\psi r|}{\big[(\partial_\Phi r)^2 + r^2(\partial_\psi r)^2\big]^{1/2}} - \frac{B}{2r^2} = \frac{1}{2}c^2 + 1 - \frac{B}{2}. \tag{32}$$

We are interested in symmetric solutions and truncate the variable Φ at some point $\Phi_\infty > 0$, so our rectangular computational domain reduces to

$$0 \le \Phi \le \Phi_\infty\,, \qquad 0 \le \psi \le \psi_S\,.$$

Together with these equations, we impose the no-flux condition

$$r = 0\,, \tag{33}$$

at the axial rod $\psi = 0$, $0 \le \Phi \le \Phi_\infty$. The symmetry condition at $\Phi = 0$, $0 \le \psi \le \psi_S$ and the truncation condition at $\Phi = \Phi_\infty$, $0 \le \psi \le \psi_S$ are specified by

$$\partial_\Phi r = 0\,. \tag{34}$$

The exact solution corresponding to a uniform stream with velocity c is given by $\Phi = c\,Z$ and $\eta = 0$, and can be re-written in terms of the new variables as $r = \sqrt{2\psi/c}$. To avoid the singularity of $\partial_\psi r$ at $\psi = 0$, we introduce another variable $\psi = \Psi^2$. The partial derivatives on ψ can be easily replaced with derivatives on Ψ in the equations to be solved.

We use a regular grid with N_p equally spaced points in Φ between 0 and Φ_∞, and M_p equally spaced points in Ψ between 0 and $\Psi_S = \sqrt{\psi_S}$ to perform the computations. We discretize the equivalent of (31) in terms of Φ and Ψ using centered differences at the interior points of this mesh and enforce the boundary conditions (32)–(34). Given B and c, the $N_p \times M_p$ nonlinear algebraic equations obtained for the $N_p \times M_p$ unknowns $r(\Phi_i, \Psi_j)$, $i = 1, \ldots, N_p$, $j = 1, \ldots, M_p$ are solved iteratively using Newton's method. The free-surface location is extracted from the converged solution as $r(\Phi, \Psi_S)$. The unknown $Z(\Phi)$ is determined by integrating numerically the second equation of (30) at $\Psi = \Psi_S$, using the trapezoidal rule. The accuracy of the numerical solution was checked by varying the numbers of grid points N_p and M_p, and by varying the truncation point Φ_∞. Most of the results presented here were obtained with $N_p = 77$, $M_p = 20$ and for various values of Φ_∞, Ψ_S ranging from 5 to 20. We have also used a version of this numerical method where the wave amplitude is fixed as the $(N_p \times M_p + 1)$-st equation and the speed c is found as the $(N_p \times M_p + 1)$-st unknown. Typically, a forced solution of small amplitude is first calculated by applying a Gaussian pressure at the free surface and then is prescribed as an initial guess to look for the branch of pure solitary waves by continuation in amplitude.

Because this finite-difference scheme generates a non-uniform spatial grid in Z, the resulting data are fitted onto the pseudo-spectral uniform grid in z by using cubic interpolation to provide the initial solution at $t = 0$. Furthermore, to comply with the periodic boundary conditions imposed by the pseudo-spectral method, the interpolated data on velocity potential $\Phi_{\min} \le \Phi \le \Phi_{\max}$ are made periodic (with zero boundary conditions) over $z_{\min} \le z \le z_{\max}$ via a linear harmonic transformation such that the initial conditions are

$$\eta(z,0) = r(\Phi, \Psi_S) - 1\,, \qquad \xi(z,0) = \Phi - \Phi_{\min} + \frac{\Phi_{\max} - \Phi_{\min}}{z_{\max} - z_{\min}}(z_{\min} - z)\,.$$

The interpolated data on the free surface r are spatially localized and thus need not be further periodized.

4. Numerical results

4.1. Convergence of the DNO

The DNO has been shown to be analytic in η under certain regularity conditions on the free surface, which implies that it can be written in terms of a convergent Taylor series expansion in η and its convergence is expected to be exponential with the truncation order. We have examined this property with the present algorithm by comparing the numerical approximation (26) of the DNO with an exact expression, based on the harmonic solution

$$\Phi = I_0(kr)\sin(kz)\,, \tag{35}$$

where, again, the time dependence is omitted because the domain is fixed in this test. Given η, an exact expression of the DNO can be obtained by inserting (35) into (10), yielding

$$\begin{aligned} G^E(\eta)\xi &= \partial_r\Phi - (\partial_z\Phi)(\partial_z\eta)\Big|_{r=1+\eta}\,, \\ &= k\Big[I_1\big(k(1+\eta)\big)\sin(kz) - (\partial_z\eta)I_0\big(k(1+\eta)\big)\cos(kz)\Big]\,. \end{aligned}$$

We will present convergence tests for two types of surface profiles, namely a sinusoidal one

$$\eta = \varepsilon\cos(kz)\,, \tag{36}$$

mimicking periodic waves, and a Gaussian one

$$\eta = \varepsilon e^{-\alpha z^2}\,, \tag{37}$$

mimicking solitary waves.

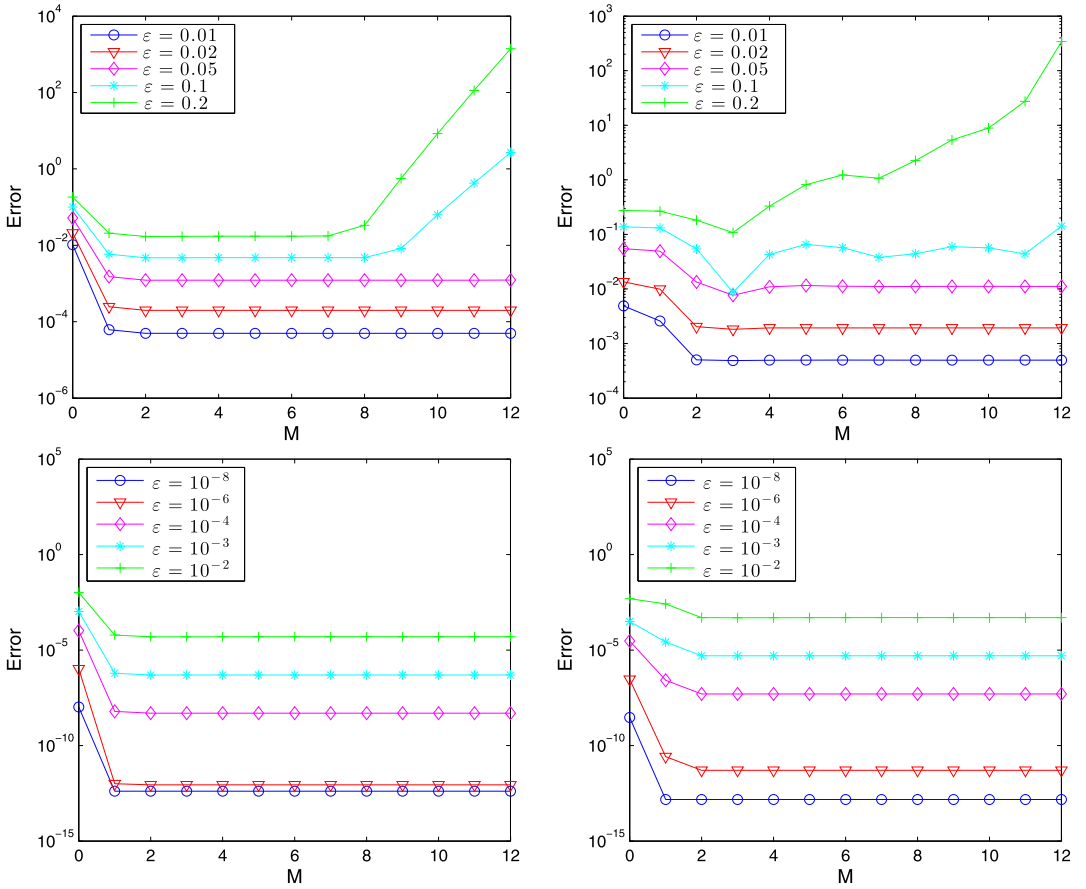

Fig. 1. Relative L^∞ error on the DNO as a function of M for a sinusoidal surface profile η of varying amplitude ε with wavenumber $k = 1$ (left) and $k = 10$ (right). The spatial resolution is $N = 1024$.

Fig. 1 shows the relative L^∞ error between G^E and G^M, i.e.

$$\text{Error} = \frac{\|G^E - G^M\|_\infty}{\|G^E\|_\infty},$$

as a function of M for different values of ε in the case of a slowly varying sinusoidal profile ($k = 1$) and a rougher one ($k = 10$). The computational domain is $[-\pi, \pi]$ with resolution $N = 1024$ (i.e. grid size $\Delta z = 0.006$). A first observation is that convergence with respect to ε is clearly demonstrated: the lower the amplitude ε, the lower the error for a fixed M. This error falls down to near machine precision for very small values of ε. However, although the errors remain overall small, their decay quickly stagnates past $M \simeq 2$. We also see that, for large amplitudes, the convergence deteriorates leading to a dramatic error growth past some critical value of M. The larger the amplitude or steepness of η (i.e. the larger ε or k), the smaller this critical value. Such a phenomenon is an illustration of numerical ill-conditioning of the series expansion (19) for the DNO that we mentioned earlier and it has been observed in other physical contexts [30,18,38].

The rapid stagnation of convergence is also related to this ill-conditioning but is more peculiar to the present axisymmetric case. Unlike the rectangular geometry with Cartesian coordinates as adopted in previous studies of the water wave problem, where the harmonic solution (18) involves a hyperbolic sine (i.e. *sinh*) function in the vertical direction and hence its successive derivatives are simply either a *cosh* or *sinh* function, here each derivative of I_0 or I_1 in (23) contains several terms whose number increases with the differentiation order. As a consequence, the number of contributions to each G_j is also further increased and, for example, we can already see that many more terms are produced in (21)–(22) when going from G_1 to G_2. Via recursion, the expression of each G_j is expected to grow fast in complexity with the order j, which may explain why the convergence saturates so early at $M \simeq 2$ as revealed in Fig. 1. This pinpoints the recursion formulas (24)–(25) for $I_0^{(n)}$ and $I_1^{(n)}$ as an additional aggravating contributor to ill-conditioning of the DNO by promoting numerical errors due to non-exact cancellation of terms. Unfortunately, we are unaware of alternate efficient ways to compute the derivatives of modified Bessel functions.

The same features are observed for a localized Gaussian profile in Fig. 2. Moreover, as illustrated with a sinusoidal profile in Fig. 3, the convergence versus M also deteriorates with increasing resolution N (while fixing ε and k). This is consistent

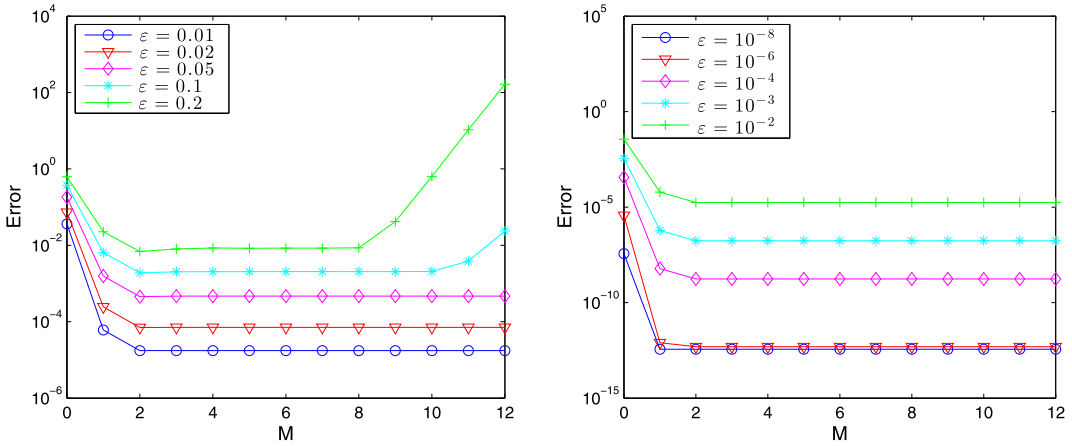

Fig. 2. Relative L^∞ error on the DNO as a function of M for a Gaussian surface profile η of varying amplitude ε with decay rate $\alpha = 5$. The spatial resolution is $N = 1024$.

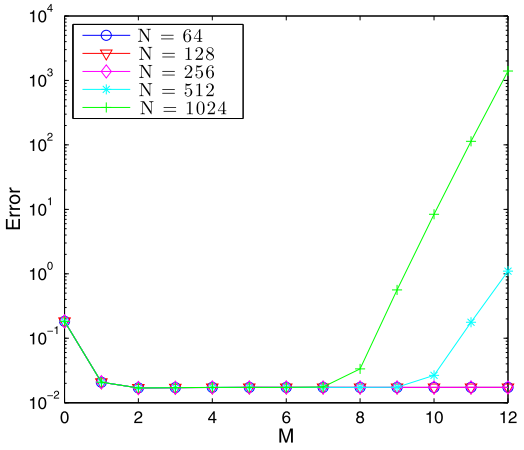

Fig. 3. Relative L^∞ error on the DNO as a function of M for a sinusoidal surface profile η of amplitude $\varepsilon = 0.2$ and wavenumber $k = 1$ with varying resolution N. The numbers of grid points $N = 64$, 128, 256, 512, 1024 correspond to grid sizes $\Delta z = 0.098$, 0.049, 0.024, 0.012, 0.006 respectively.

with our previous statement that the presence of Fourier multipliers in (23) tend to amplify numerical errors in the high Fourier modes. For fine resolutions, this error amplification is particularly severe past some critical value of M. Below this critical value, the convergence rate quickly stagnates as noted before and is pretty much identical in all cases. For low resolutions or low amplitudes, it is nonetheless a little comfort that the errors only stagnate and remain small rather than quickly growing with M. This helps justify that our numerical method could still be employed to simulate the present ferrofluid problem with reasonable accuracy by specifying suitable values of M and N.

We have also examined the influence of de-aliasing on the convergence of the DNO, as depicted in Fig. 4 for $\varepsilon = 0.1$, $k = 10$ and $N = 1024$. It can be seen that the loss of convergence in the aliased computation occurs sooner (at $M \simeq 10$) than in the de-aliased one. This indicates that the zero-padding technique is effective at reducing aliasing errors in the evaluation of the DNO. Needless to say that it is important to minimize errors as much as possible at this stage since they may quickly accumulate during the time integration owing to the nonlinearity in the governing equations.

4.2. Solitary waves

Solitary waves on the surface of a ferrofluid jet have been the subject of several recent studies ranging from theoretical [34] to experimental [6] and numerical [5]. In particular, Rannacher and Engel [34] derived a KdV equation for the present ferrofluid problem and examined a case of overtaking collision with the two-soliton solution of this weakly nonlinear model. Here we extend their results to the highly nonlinear regime by performing time-dependent simulations of (15)–(16). Doing so helps validate not only the proposed algorithm that solves the time-evolution problem but also the finite-difference method of [5] which independently generates the initial condition. Because the present paper is focused on the development and testing of our DNO approach, we only show illustrative examples and postpone a more in-depth study of solitary wave collisions to a future publication. For the interested reader, such an investigation in the context of water waves can be

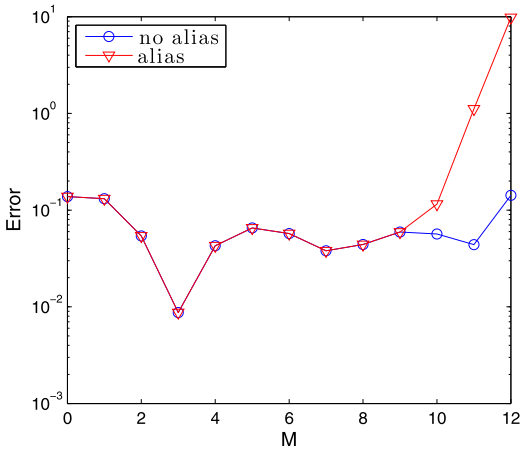

Fig. 4. Relative L^∞ error on the DNO as a function of M for a sinusoidal surface profile η of amplitude $\varepsilon = 0.1$ and wavenumber $k = 10$ with (blue circles) and without (red triangles) de-aliasing. The spatial resolution is $N = 1024$. (For interpretation of the references to color in this figure, the reader is referred to the web version of this article.)

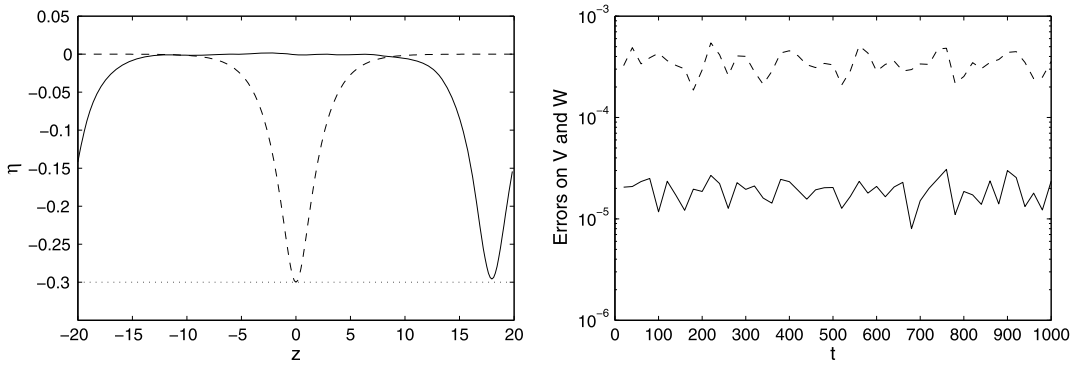

Fig. 5. Solitary wave of depression with amplitude $\varepsilon = 0.3$ for $B = 2.5$. Left: profiles at $t = 0$ (dashed line) and $t = 1000$ (solid line). Right: relative errors on mass V (dashed line) and volume W (solid line) versus time.

found in [10]. Based on the convergence tests shown in the previous section, we have found it sufficient to use $M = 2$ (with de-aliasing) for all the numerical simulations to be presented below. We have checked that using a higher value of M gives similar results.

Following the KdV analysis [3,34], we first consider the range $3/2 < B < 9$ that supports solitary waves of depression with speed $c < c_0$ and then the narrower range $1 < B < 3/2$ for solitary waves of elevation with $c < c_0$. The first experiment concerns the free propagation of a single solitary wave, in which case the solution is expected to evolve in time without change of shape and speed. Fig. 5 plots the initial condition of η at $t = 0$ together with its counterpart at a much later time $t = 1000 \gg \tau$ from the simulation of a depression solitary wave with amplitude $\varepsilon = 0.3$ for $B = 2.5$. The spatial resolution is $\Delta z = 0.15$ ($N = 256$ grid points over $-20 \le z \le 20$). Apart from the translation in z, we see that the two profiles look pretty much identical. It is because of the periodic boundary conditions that the initial and final pulses end up being located relatively close together. Over the time interval $[0, 1000]$, the solution has actually traveled several times through the computational domain $[-20, 20]$. Fig. 5 also indicates that mass (5) and volume (6) are well conserved throughout the entire simulation, with relative errors

$$\frac{\Delta V(t)}{V_0} = \left| \frac{V(t) - V_0}{V_0} \right|, \qquad \frac{\Delta W(t)}{W_0} = \left| \frac{W(t) - W_0}{W_0} \right|,$$

of order $O(10^{-4})$ and $O(10^{-5})$ respectively, where V_0 and W_0 denote the initial values of V and W at $t = 0$, and furthermore these errors exhibit no global increasing or decreasing trend over time. The integrals in (5) and (6) were evaluated by the trapezoidal rule. Because this long computation required filtering (which is typically needed for $\varepsilon > 0.1$), it supports the fact that our filtering technique is effective at suppressing numerical instabilities while keeping the solution's spectrum essentially unaffected. The small reduction in wave amplitude discernible from Fig. 5 at $t = 1000$ is partly attributable to filtering.

To more closely check the numerical preservation of solitary wave profiles over time, Fig. 6 shows their superposition in such a way that their troughs coincide. For $\varepsilon = 0.3$, the two profiles at $t = 0$ and $t = 1000$ are pretty much indistinguishable

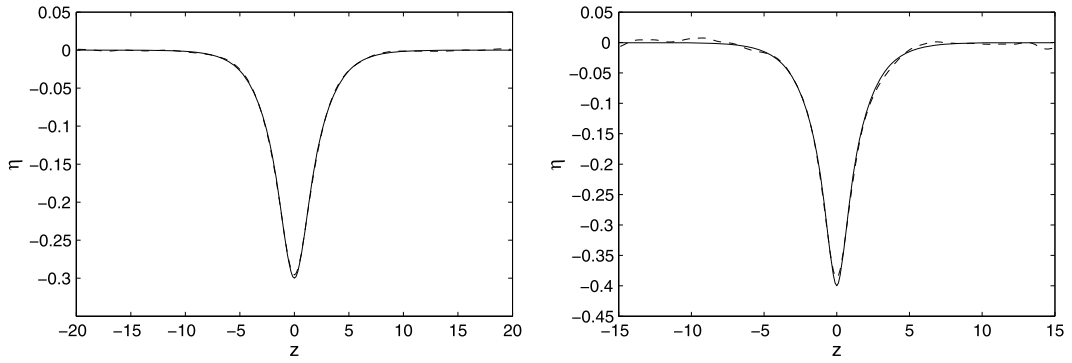

Fig. 6. Superposition of solitary wave profiles at $t = 0$ (solid line) and $t = 1000$ (dashed line) for $B = 2.5$. Left: $\varepsilon = 0.3$. Right: $\varepsilon = 0.4$.

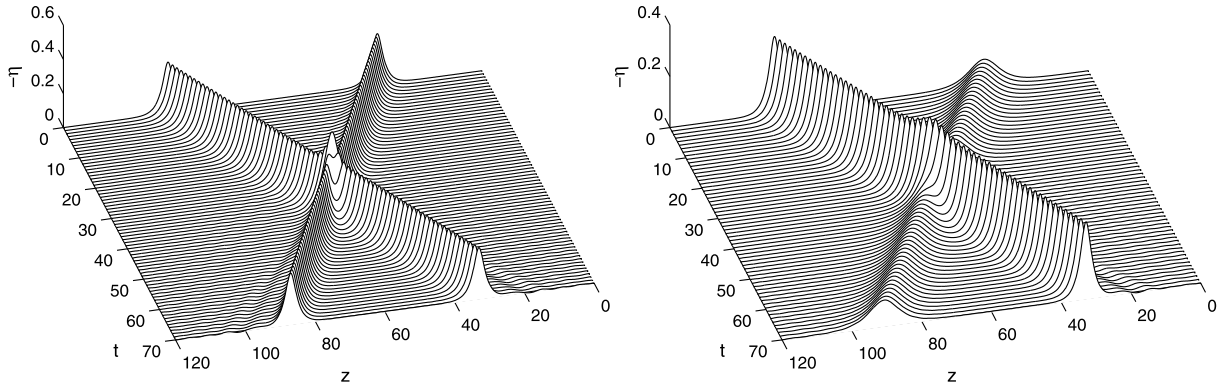

Fig. 7. Head-on collision of two solitary waves of depression for $B = 2.5$. Reversed profiles are shown. Left: equal amplitudes $\varepsilon = 0.3$. Right: different amplitudes $\varepsilon = 0.1$ and $\varepsilon = 0.3$.

to graphical accuracy while, for $\varepsilon = 0.4$, small discrepancies are noticeable at the bottom and on both sides of the wave trough. As ε is increased, the computed wave tends to decay and lose coherency over time by emitting radiation. More quantitatively, the relative L^2 error between the two profiles at $t = 0$ and $t = 1000$ is found to be 1.4×10^{-2}, 4.3×10^{-2} for $\varepsilon = 0.3$, 0.4 respectively. For lower wave amplitudes, the errors on wave profile and mass/volume conservation are even smaller, so the results are not shown here for convenience. For $\varepsilon > 0.4$ in this magnetic regime, the numerical solution was observed to disperse or the code broke down after a short run time.

We further examine properties of solitary waves in this ferrofluid problem by simulating their pairwise collisions. From the existing literature, it was not known whether such collisions are elastic in the fully nonlinear case and, if not, to what extent they are inelastic. Physically, this has implications for the nonlinear stability of ferrofluid jets and their potential applications. Fig. 7 depicts the (z,t)-diagram for the head-on collision of two solitary waves moving in opposite directions. Two situations are considered: a symmetric collision of two waves with equal amplitude $\varepsilon = 0.3$, and an asymmetric collision of two waves with different amplitudes $\varepsilon = 0.1$ and 0.3. For clarity, the reversed profile of these depression solitary waves is shown in Fig. 7. In both cases, the spatial resolution is $\Delta z = 0.11$ ($N = 1024$ grid points over $0 \le z \le 120$), and the initial condition is simply the superposition of two individual solutions generated by the finite-difference scheme. This is justified by the fact that their initial locations are chosen to be sufficiently well separated from each other. Note that the direction of wave propagation (left or right) can be set initially by simply changing the sign of the velocity potential ξ. At first glance, the collision patterns look similar to those occurring in e.g. the water wave problem [10] but there are notable differences as discussed in more detail next.

Closer examination of the symmetric head-on collision with $\varepsilon = 0.3$ is presented in Fig. 8 displaying snapshots of the free surface at various times. As a reference, the numerical solution is compared with the superposition of two individual counter-propagating KdV solitons

$$\eta(z,t) = \frac{3c_1}{\kappa}\operatorname{sech}^2\left[\sqrt{\frac{c_1}{4\sigma}}\Big(z - z_1 - (c_1 + c_0)t\Big)\right] + \frac{3c_2}{\kappa}\operatorname{sech}^2\left[\sqrt{\frac{c_2}{4\sigma}}\Big(z - z_2 + (c_2 + c_0)t\Big)\right], \tag{38}$$

where z_1, z_2 are the initial locations of the two pulses, c_0 is given by (8),

$$\kappa = \frac{2B-3}{4c_0}, \qquad \sigma = \frac{B-9}{32c_0}, \qquad c_i = \operatorname{sgn}(\sigma)\left|\frac{\varepsilon_i \kappa}{3}\right|, \qquad i = \{1,2\},$$

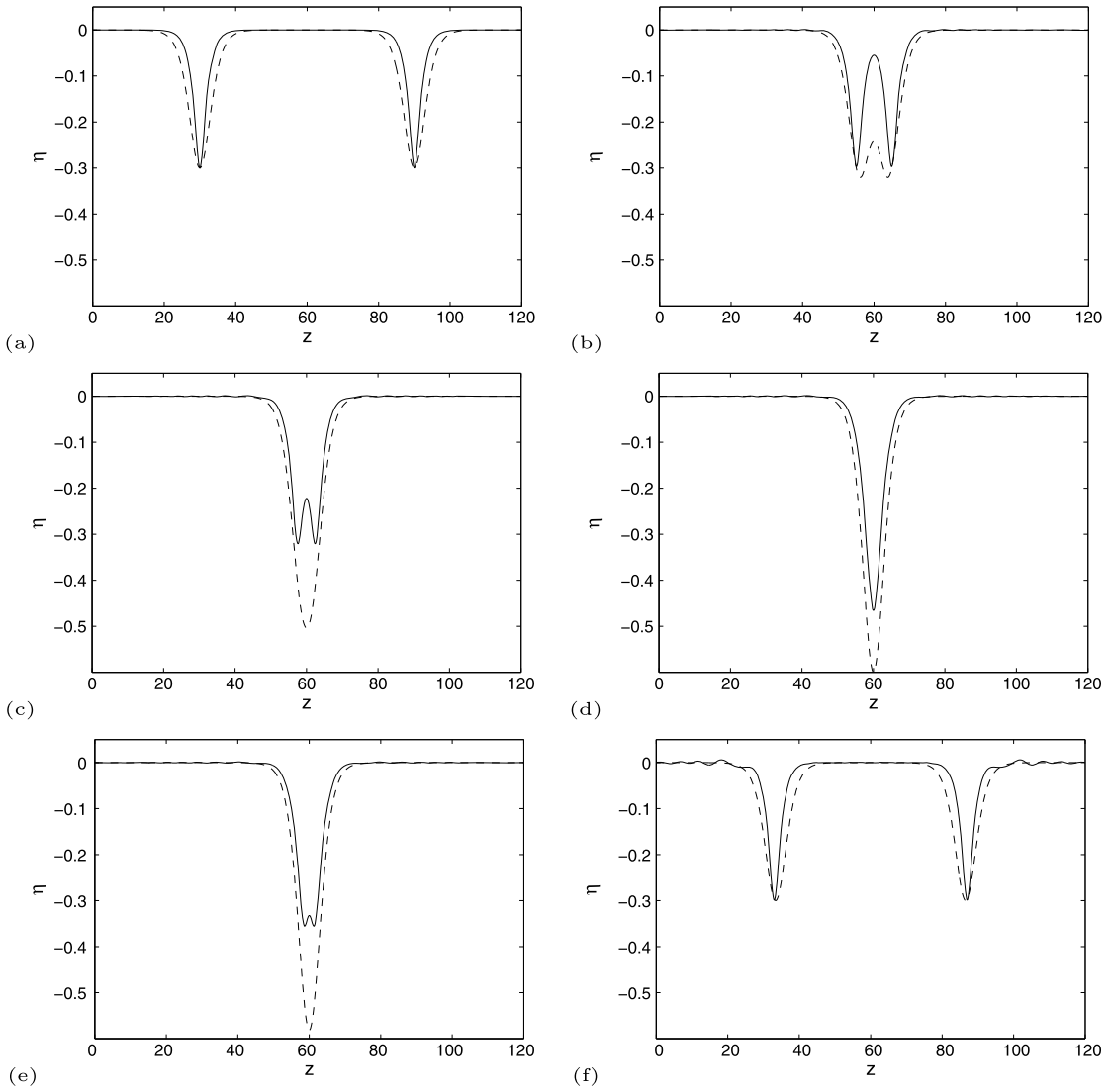

Fig. 8. Head-on collision of two solitary waves of depression with equal amplitude $\varepsilon = 0.3$ for $B = 2.5$. The numerical solution is represented by a solid line while the superposition of two KdV solitons is represented by a dashed line. Profiles at $t = 0$ (a), 32 (b), 35 (c), 37 (d), 38 (e) and 70 (f) are shown.

and here $\varepsilon_1 = \varepsilon_2 = 0.3$ [34]. Equation (38) reveals why solitary waves are expected to be of depression in the range $3/2 < B < 9$ since $\kappa > 0$ and $\sigma < 0$, while they should be of elevation for $1 < B < 3/2$ since both $\kappa < 0$ and $\sigma < 0$. This formula also predicts that the solitary wave speed should be less than the linear phase speed c_0 in both ranges of B since $\sigma < 0$ and hence $c_i < 0$ for $B < 9$, which implies that $c_i + c_0 < c_0$. In particular, the lower the wave amplitude, the higher the speed which gets closer to c_0.

These weakly nonlinear predictions are qualitatively verified by our numerical simulations (see also the discussion for elevation waves below). However, on the quantitative level, "fully nonlinear" solutions tend to be steeper than KdV solitons for the same amplitude. As expected from the superposition (38), the KdV approximation can reach a maximum amplitude twice as large as the initial one (at $t = 37$ in Fig. 8), while the numerical solution does not get so deep. This phenomenon contrasts with the water wave problem where colliding solitary waves attain a maximum amplitude slightly higher than the sum of the initial ones. Moreover, consistent with a previous statement, the interaction is inelastic and induces small-amplitude long residual waves that develop ahead of (rather than trailing behind) the two separating pulses because they travel faster at the linear speed c_0. These residual waves can be clearly seen at $t = 70$ in Fig. 8 and their wake-like pattern can also be identified in the (z, t)-diagram of Fig. 7. We believe their nature is physical, rather than being spurious numerical excitations, because the collision takes place over a relatively short interval of time and these residual waves distinctively arise after it. We have also checked their presence in computations with a finer resolution or a higher value of M. Not surprisingly, another observation from Fig. 8 is the occurrence of a phase shift due to the interaction, which is indicated by the slight mismatch between KdV and numerical profiles at $t = 70$. Similar results were obtained for the

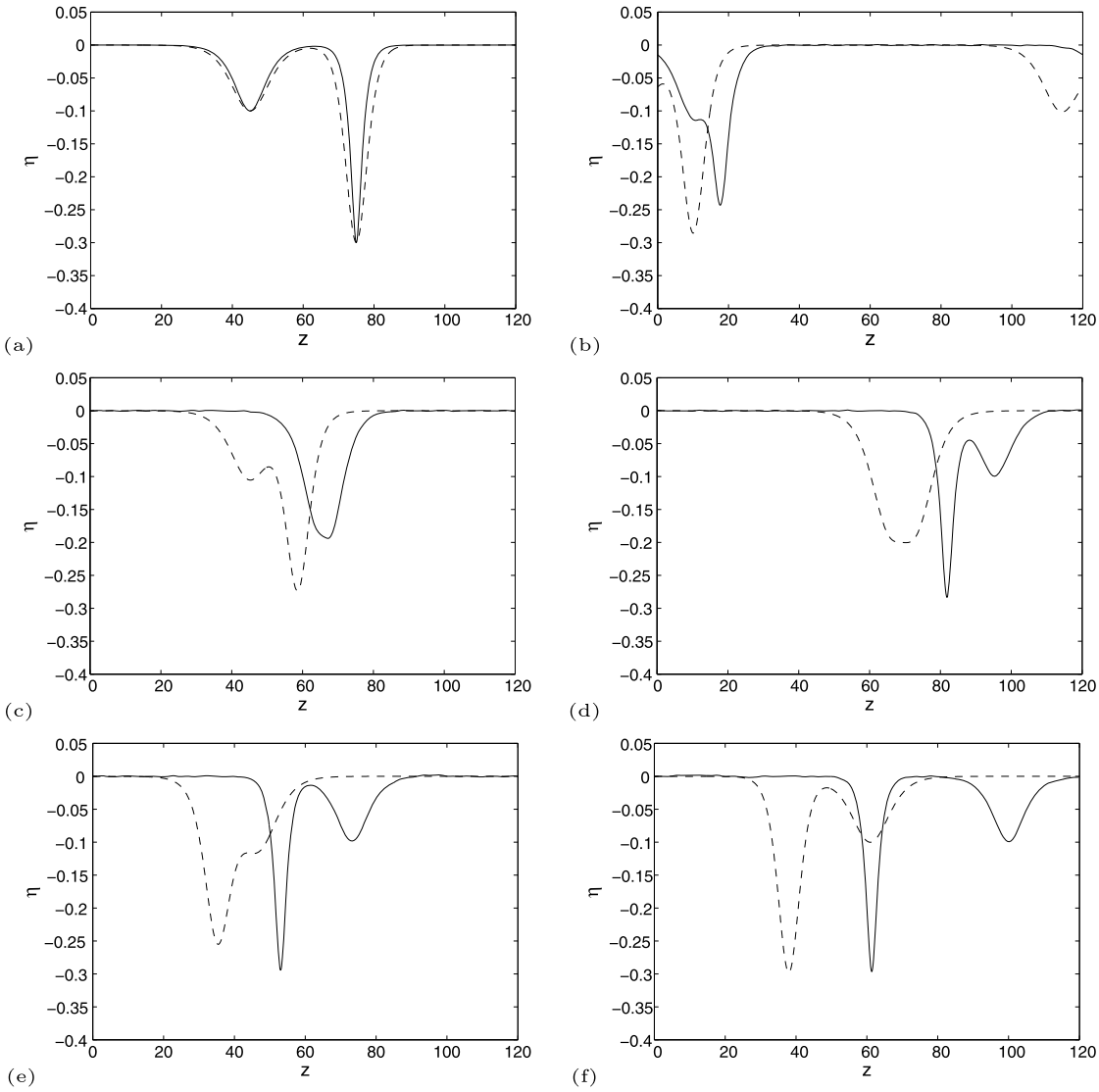

Fig. 9. Overtaking collision of two solitary waves of depression with amplitudes $\varepsilon = 0.1$ and $\varepsilon = 0.3$ for $B = 2.5$. The numerical solution is represented by a solid line while the KdV two-soliton solution is represented by a dashed line. Wave propagation is from left to right. Profiles at $t = 0$ (a), 365 (b), 425 (c), 590 (d), 700 (e) and 1000 (f) are shown.

asymmetric head-on collision and, understandably, a more pronounced residual wave tends to develop near the larger pulse as depicted in Fig. 7.

In addition to head-on interactions, we have also simulated overtaking cases where both solitary waves move in the same direction, and an example is provided in Fig. 9. Clearly, the two waves must now be of different amplitudes so that their speeds are different otherwise one cannot overtake the other. Fig. 9 shows snapshots of such a collision for $\varepsilon = 0.1$ and $\varepsilon = 0.3$. This time, the computation is compared with the one-way KdV two-soliton solution

$$\eta(z,t) = 4\frac{\delta_1\gamma_1^2 + \delta_2\gamma_2^2 + 2\delta_1\delta_2(\gamma_1-\gamma_2)^2 + (\delta_1\delta_2^2\gamma_1^2 + \delta_1^2\delta_2\gamma_2^2)(\gamma_1-\gamma_2)^2/(\gamma_1+\gamma_2)^2}{\left[1+\delta_1+\delta_2+\delta_1\delta_2(\gamma_1-\gamma_2)^2/(\gamma_1+\gamma_2)^2\right]^2},$$

where

$$\delta_1 = \exp\left[-\sqrt{\frac{c_1}{\sigma}}\Big((z-z_1-(c_1+c_0)t\Big)\right], \qquad \delta_2 = \exp\left[\sqrt{\frac{c_2}{\sigma}}\Big((z-z_2-(c_2+c_0)t\Big)\right],$$

and $\gamma_i^2 = 3c_i/\kappa$ $(i = 1, 2)$ as derived by Rannacher and Engel [34]. The parameters c_i, κ and σ are the same as those defined in (38). As stated earlier (unlike water waves), it is the smaller solitary wave that catches up with the larger

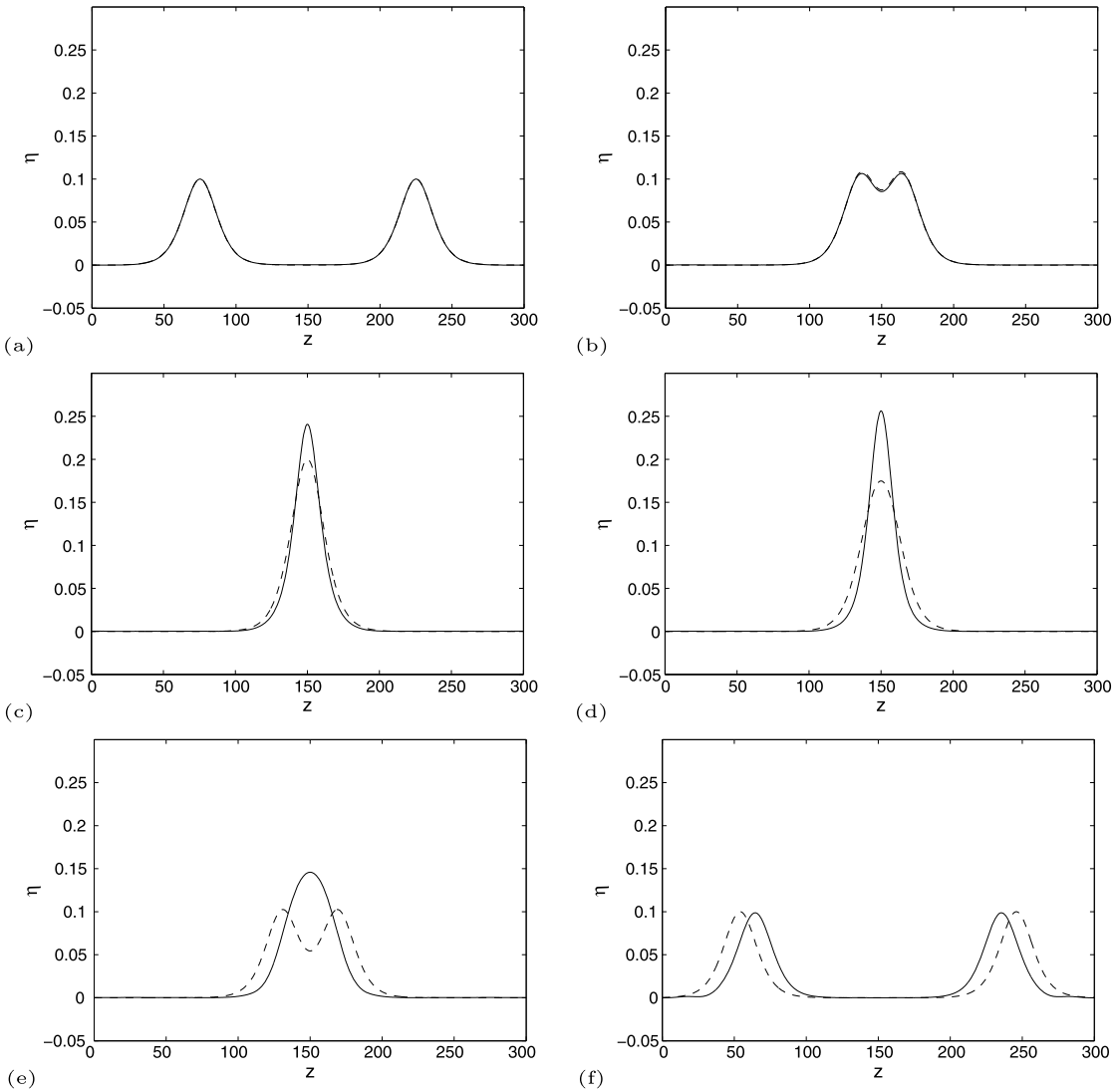

Fig. 10. Head-on collision of two solitary waves of elevation with equal amplitude $\varepsilon = 0.1$ for $B = 1.25$. The numerical solution is represented by a solid line while the superposition of two KdV solitons is represented by a dashed line. Profiles at $t = 0$ (a), 176 (b), 220 (c), 236 (d), 276 (e) and 500 (f) are shown.

one and overtakes it. The first snapshot of Fig. 9 also confirms the expectation that the lower the wave amplitude, the closer the KdV approximation to the numerical solution. Because overtaking collisions take place over a longer time scale than head-on collisions, differences between KdV and "fully nonlinear" evolutions get more pronounced. In particular, the interaction process predicted by the KdV equation is significantly delayed compared to the numerical one: it is delayed both in the overall evolution and propagation. However, apart from this delay, Fig. 9 suggests that the main features are well reproduced by the KdV solution. The two interacting waves seem to pass each other without amplitude increase. When they merge at $t = 425$, the resulting profile looks like being their average rather than a superposition. After the collision, they tend to separate into two individual solitary waves resembling the initial ones, with negligible residual. This close resemblance with the initial condition is clearly displayed in Fig. 9 at the late time $t = 1000$ and further demonstrates the good performance of our algorithm.

We turn our attention to solitary waves of elevation for $B = 1.25$ in the range $1 < B < 3/2$. We have again checked that a single wave of this type propagates with negligible change in shape and speed if its amplitude is not too large, and this is not reported here for convenience. Note that, for a given amplitude, a solitary wave of elevation for $B = 1.25$ is found to be significantly broader than the depression one for $B = 2.5$. Fig. 10 displays snapshots during the head-on collision of two elevation waves with equal amplitude $\varepsilon = 0.1$. The spatial resolution is $\Delta z = 0.14$ ($N = 2048$ grid points over $0 \le z \le 300$), and the initial condition is set up as before. We first observe that the KdV formula (38) is quite a good approximation to these solitary waves at $t = 0$. It also reproduces well their shape during the early stages of the interaction and later during

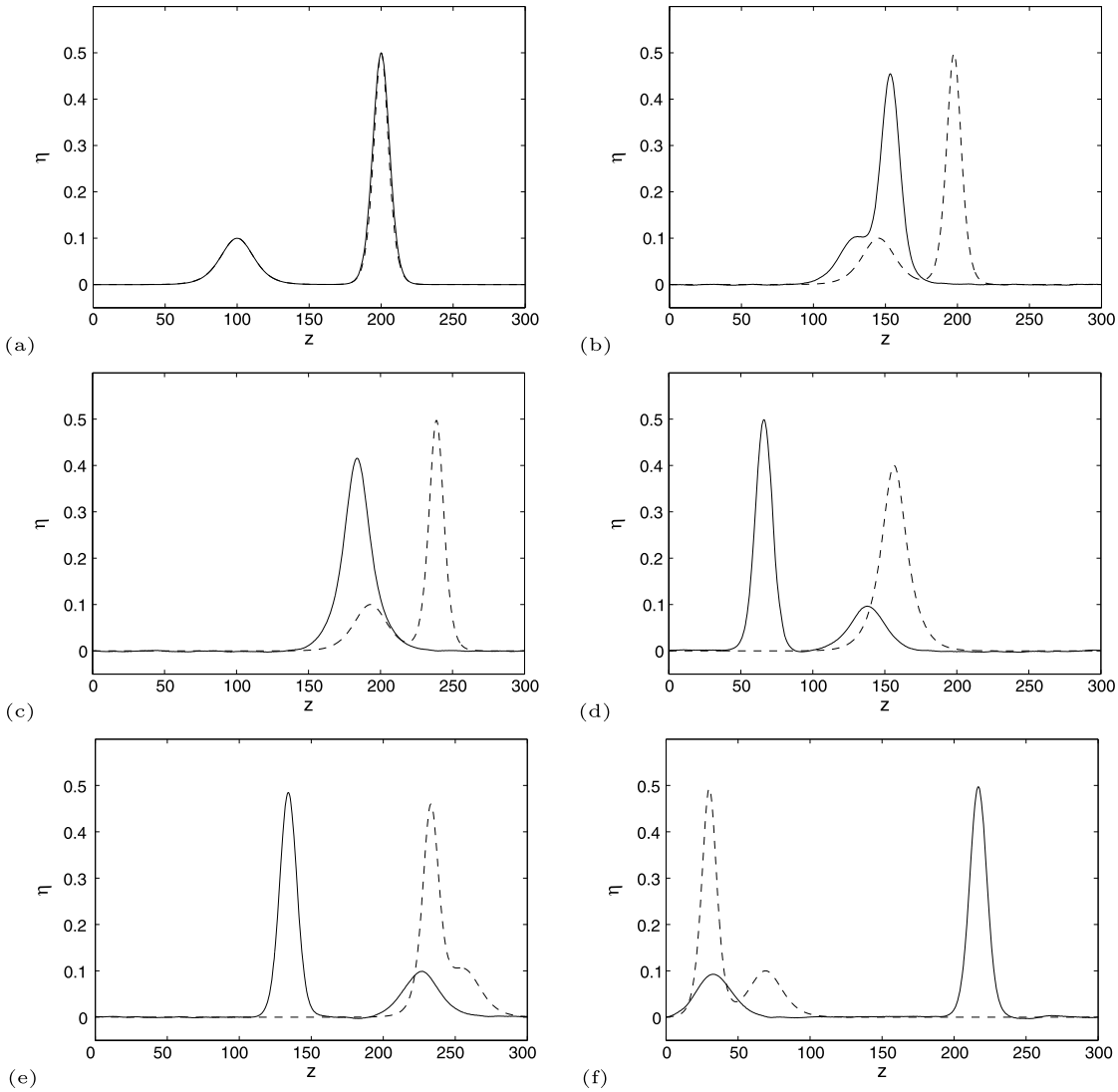

Fig. 11. Overtaking collision of two solitary waves of elevation with amplitudes $\varepsilon = 0.1$ and $\varepsilon = 0.5$ for $B = 1.25$. The numerical solution is represented by a solid line while the KdV two-soliton solution is represented by a dashed line. Wave propagation is from left to right. Profiles at $t = 0$ (a), 1010 (b), 1150 (c), 1900 (d), 2170 (e) and 2500 (f) are shown.

the separation. However, in contrast to the previous regime $B = 2.5$, the numerical solution can now reach a maximum amplitude > 0.2 (well beyond the sum of the two initial amplitudes), as illustrated in Fig. 10 at $t = 236$. Small residual waves are again produced by the collision but are barely discernible in front of each exiting pulse.

An example of overtaking collision between two solitary waves of elevation with amplitudes $\varepsilon = 0.1$ and $\varepsilon = 0.5$ is provided in Fig. 11. Note that $\varepsilon = 0.5$ is quite a large amplitude relative to the mean fluid depth $a = 1$ (in dimensionless units), nonetheless the corresponding pulse is seen to still match the KdV approximation well at $t = 0$. Observations similar to those for $B = 2.5$ can be made here and, in particular, the solution's amplitude turns out to be less than the largest initial amplitude at the time of complete merging, as shown in Fig. 11 at $t = 1150$ when $\|\eta\|_\infty \simeq 0.4 < 0.5$. A major difference with the depression case is that, although the numerical process of interaction occurs faster than the one predicted by the KdV equation, its overall propagation is slower (i.e. the mean location of the numerical profile tends to trail behind that of the KdV profile). When looking at Fig. 11, recall that the waves have traveled multiple times through the computational domain due to the periodic boundary conditions. The asymptotic state as $t \to +\infty$ is again two separate solitary waves almost identical to the initial ones coexisting with some small radiative background. Many features occurring here bear close resemblance with those observed in the water wave problem [10] and, for future work, it would be worth identifying more clearly the various mechanisms and scenarios involved. Finally, it is emphasized that simulation of overtaking collisions is a particularly discriminating test because the numerical model must be able to accurately capture both the dispersive and nonlinear effects over a long period of time.

5. Conclusions

We have explored the possibility of using a boundary-perturbation technique to simulate the propagation of axisymmetric nonlinear waves on the surface of a ferrofluid jet. Our new numerical approach is based on the reduction of the original Laplace problem to a lower-dimensional system involving surface variables alone. This is achieved by introducing the DNO which is expressed in terms of a convergent Taylor series expansion about the uniform cylindrical geometry of the jet. A recursion formula was derived to evaluate this Taylor series up to an arbitrary order, with each term being given as a sum of concatenations of Fourier multipliers with powers of the surface deformation. This allows the DNO to be efficiently computed by a pseudo-spectral method using the FFT, and thus makes our boundary-perturbation approach especially suitable for time-evolution simulations. In the axisymmetric case, these Fourier multipliers involve modified Bessel functions in the radial direction.

We have shown extensive numerical tests on the convergence of the DNO as a function of the truncation order M for various surface profiles, surface amplitudes and spatial resolutions. Effects of de-aliasing were also investigated. Although the errors remain overall small, their decrease is not found to be exponential in M, unlike what could be expected from the analyticity property of the DNO. Rather, our tests indicate that the convergence quickly stagnates past $M \simeq 2$ and even deteriorates past a critical higher value of M for large surface deformations or fine spatial resolutions. Although the latter behavior is known to be related to ill-conditioning of the DNO in its series form, the former behavior is an issue believed to be more peculiar to the present axisymmetric case. Indeed, the recursion formula for our DNO involves derivatives of modified Bessel functions that are themselves determined recursively and this tends to amplify numerical errors as M increases.

Despite these numerical issues on the DNO, we have found that our algorithm gives quite satisfactory results when applied to solving the initial-value problem. We have extended the results of [34] and [5] by simulating the long-time propagation and pairwise collisions of solitary wave solutions in the highly nonlinear regime. Both depression and elevation waves were examined by varying the magnetic Bond number B, and comparisons with KdV predictions were also made. In all cases that we have considered, the collisions are found to be inelastic, generating small residual waves ahead of the separating pulses. The significance of these residual waves depends on the collision type and on the initial amplitude of the colliding solitary waves. In the overtaking case, the interaction is relatively weak and produces residual waves that are barely noticeable. In the head-on case, the interaction is typically stronger leading to more radiation but the maximum amplitude reached may be slightly less or more than the sum of the two initial amplitudes depending on whether the solitary waves are of depression or elevation.

Our preliminary results together with those of [5] suggest that this ferrofluid problem has a rich physical nature and thus further investigation is called for to better characterize the observed phenomena. A magnetic regime that we have not described here is $B \geq 9$ where solutions are particularly nonlinear and solitary waves may be unstable. Their numerical simulation requires special care and is envisioned for future work. In addition, it would be of interest to extend our numerical model to the more realistic situation $0 < b < 1$ (i.e. an inner conducting wire of small but finite thickness) and explore whether there are major differences in dynamical behavior as compared with $b = 0$. Adapting the procedure of [11,13], we might also consider the configuration where the jet surface lies between two fluid layers (rather than assuming vacuum in the outer region) so as to more closely describe the experimental set-up of [6] and possibly compare with their data.

Acknowledgements

P. Guyenne is partially supported by the Simons Foundation under grant 246170. E.I. Părău is partially supported by the EPSRC under grant EP/J019305/1. P. Guyenne thanks the Department of Mathematics & Computer Science at Chulalongkorn University and Dr. Khamron Mekchay for their hospitality and assistance during a visit in the spring and summer 2016. Both authors thank the Isaac Newton Institute for Mathematical Sciences (Cambridge, UK) for its hospitality during the Theory of Water Waves program in the summer 2014.

References

[1] M. Abramowitz, I.A. Stegun, Handbook of Mathematical Functions with Formulas, Graphs, and Mathematical Tables, Dover, New York, 1972.
[2] V.I. Arkhipenko, Y.D. Barkov, Experimental study of the breakdown of the cylindrical layer of a magnetizable fluid under the action of magnetic forces, J. Appl. Mech. Tech. Phys. 21 (1980) 98–105.
[3] V.G. Bashtovoi, R. Foigel, Solitary and cnoidal waves in ferrofluid, Magnetohydrodynamics 19 (1983) 160–165.
[4] V.G. Bashtovoi, A. Rex, R. Foigel, Some nonlinear wave processes in a magnetic fluid, J. Magn. Magn. Mater. 39 (1983) 115–118.
[5] M.G. Blyth, E.I. Părău, Solitary waves on a ferrofluid jet, J. Fluid Mech. 750 (2014) 401–420.
[6] E. Bourdin, J.-C. Bacri, E. Falcon, Observation of axisymmetric solitary waves on the surface of a ferrofluid, Phys. Rev. Lett. 104 (2010) 094502.
[7] C. Canuto, M.Y. Hussaini, A. Quarteroni, T.A. Zang, Spectral Methods in Fluid Dynamics, Springer-Verlag, Berlin, 1987.
[8] R. Coifman, Y. Meyer, Nonlinear harmonic analysis and analytic dependence, Proc. Symp. Pure Math. 43 (1985) 71–78.
[9] W. Craig, Transformation theory of Hamiltonian PDE and the problem of water waves, in: Hamiltonian Dynamical Systems and Applications, Springer, Dordrecht, 2008, pp. 67–83.
[10] W. Craig, P. Guyenne, J. Hammack, D. Henderson, C. Sulem, Solitary water wave interactions, Phys. Fluids 18 (2006) 057106.
[11] W. Craig, P. Guyenne, H. Kalisch, Hamiltonian long wave expansions for free surfaces and interfaces, Commun. Pure Appl. Math. 58 (2005) 1587–1641.
[12] W. Craig, P. Guyenne, C. Sulem, Hamiltonian higher-order nonlinear Schrödinger equations for broader-banded waves on deep water, Eur. J. Mech. B/Fluids 32 (2012) 22–31.

[13] W. Craig, P. Guyenne, C. Sulem, The surface signature of internal waves, J. Fluid Mech. 710 (2012) 277–303.
[14] W. Craig, D.P. Nicholls, Traveling gravity water waves in two and three dimensions, Eur. J. Mech. B/Fluids 21 (2002) 615–641.
[15] W. Craig, U. Schanz, C. Sulem, The modulational regime of three-dimensional water waves and the Davey–Stewartson system, Ann. Inst. Henri Poincaré Anal. Non Linéaire 14 (1997) 615–667.
[16] W. Craig, C. Sulem, Numerical simulation of gravity waves, J. Comput. Phys. 108 (1993) 73–83.
[17] R. de la Llave, P. Panayotaros, Gravity waves on the surface of the sphere, J. Nonlinear Sci. 6 (1996) 147–167.
[18] Q. Fang, D.P. Nicholls, J. Shen, A stable, high-order method for three-dimensional, bounded-obstacle, acoustic scattering, J. Comput. Phys. 224 (2007) 1145–1169.
[19] Z. Fang, D.P. Nicholls, An operator expansions method for computing Dirichlet–Neumann operators in linear elastodynamics, J. Comput. Phys. 272 (2014) 266–278.
[20] P. Guyenne, D.P. Nicholls, A high-order spectral method for nonlinear water waves over moving bottom topography, SIAM J. Sci. Comput. 30 (2007) 81–101.
[21] P. Guyenne, E.I. Părău, Computations of fully nonlinear hydroelastic solitary waves on deep water, J. Fluid Mech. 713 (2012) 307–329.
[22] P. Guyenne, E.I. Părău, Finite-depth effects on solitary waves in a floating ice sheet, J. Fluids Struct. 49 (2014) 242–262.
[23] T.Y. Hou, R. Li, Computing nearly singular solutions using pseudo-spectral methods, J. Comput. Phys. 226 (2007) 379–397.
[24] T.Y. Hou, J.S. Lowengrub, M.J. Shelley, Removing the stiffness from interfacial flows with surface tension, J. Comput. Phys. 114 (1994) 312–338.
[25] B. Hu, D.P. Nicholls, Analyticity of Dirichlet–Neumann operators on Hölder and Lipschitz domains, SIAM J. Math. Anal. 37 (2005) 302–320.
[26] R.W. Jeppson, Inverse formulation and finite difference solution for flow from a circular orifice, J. Fluid Mech. 40 (1970) 215–223.
[27] D.M. Milder, An improved formalism for wave scattering from rough surfaces, J. Acoust. Soc. Am. 89 (1991) 529–541.
[28] D.P. Nicholls, N. Nigam, Exact non-reflecting boundary conditions on general domains, J. Comput. Phys. 194 (2004) 278–303.
[29] D.P. Nicholls, F. Reitich, A new approach to analyticity of Dirichlet–Neumann operators, Proc. R. Soc. Edinb. A 131 (2001) 1411–1433.
[30] D.P. Nicholls, F. Reitich, Stability of high-order perturbative methods for the computation of Dirichlet–Neumann operators, J. Comput. Phys. 170 (2001) 276–298.
[31] J. Philip, G. Prakash, T. Jayakumar, P. Kalyanasundaram, B. Raj, Effect of polymer–surfactant association on colloidal force, Phys. Rev. E 66 (2002) 011406.
[32] W.H. Press, S.A. Teukolsky, W.T. Vetterling, B.P. Flannery, Numerical Recipes in C, Cambridge University Press, Cambridge, 1992.
[33] K. Raj, B. Moskowitz, R. Casciari, Advances in ferrofluid technology, J. Magn. Magn. Mater. 143 (1995) 174–180.
[34] D. Rannacher, A. Engel, Cylindrical Korteweg–de Vries solitons on a ferrofluid surface, New J. Phys. 8 (2006) 108–123.
[35] J.W. Rayleigh, On the instability of jets, Proc. Lond. Math. Soc. 10 (1878) 4–13.
[36] C. Scherer, A.M. Figueiredo Neto, Ferrofluids: properties and applications, Brazilian J. Phys. 35 (2005) 718–727.
[37] J.-M. Vanden-Broeck, T. Miloh, B. Spivack, Axisymmetric capillary waves, Wave Motion 27 (1998) 245–256.
[38] L. Xu, P. Guyenne, Numerical simulation of three-dimensional nonlinear water waves, J. Comput. Phys. 228 (2009) 8446–8466.